

Layer Decoupling in Twisted Bilayer WSe₂ Uncovered by Automated Dark-Field Tomography

A. Nakamura^{1,2}, Y. Chiashi^{2,†}, T. Shimojima^{1,‡}, Y. Tanaka², S. Akatsuka², M. Sakano^{2,§},
S. Masubuchi³, T. Machida³, K. Watanabe⁴, T. Taniguchi⁵, and K. Ishizaka^{1,2}

¹RIKEN Center for Emergent Matter Science, Wako, Saitama 351-0198, Japan.

²Quantum-Phase Electronics Center and Department of Applied Physics, The University of Tokyo, Hongo, Tokyo 113-8656, Japan.

³Institute of Industrial Science, The University of Tokyo, Meguro, Tokyo 153-8505, Japan.

⁴Research Center for Electronic and Optical Materials, National Institute for Materials Science, 1-1 Namiki, Tsukuba 305-0044, Japan

⁵Research Center for Materials Nanoarchitectonics, National Institute for Materials Science, 1-1 Namiki, Tsukuba 305-0044, Japan

Present address:

[†]National Institute of Advanced Industrial Science and Technology, Tsukuba, Ibaraki, 305-8568, Japan

[‡]Department of Physics, Nagoya University, Furo-cho, Aichi 464-8601, Japan

[§]Graduate School of Informatics and Engineering, The University of Electro-Communications, Chofu-gaoka, Tokyo 182-8585, Japan

Abstract

Twisted bilayer systems host a wealth of emergent phenomena, such as flat-band superconductivity, ferromagnetism, and ferroelectricity, arising from moiré superlattices and unconventional interlayer coupling. Despite their central role, direct and quantitative access to the out-of-plane atomic structure in these systems has remained elusive due to their nanoscale dimensions. Here, we introduce an automated dark-field electron tomography technique that enables three-dimensional structural analysis of atomically thin materials with sub-ångström precision. Applying this method to twisted bilayer WSe₂, we uncover a significant expansion of the interlayer spacing compared to the bulk configuration, exceeding 0.1 Å, along with a remarkable temperature-driven interlayer decoupling unique to the twisted bilayer. Ultrafast measurement further reveals optically induced interlayer separation of ~0.2 Å on the picosecond timescale, attributed to transient exciton formation. These findings not only establish a powerful approach for visualizing hidden out-of-plane structures in atomically thin micro-flake materials, but also uncover the intrinsic fragility and dynamical tunability of interlayer coupling in moiré-engineered 2-dimensional materials.

Twisted bilayers of van der Waals materials have opened new frontiers in condensed matter physics, offering a versatile platform for realizing strongly correlated, topological, and ferroelectric phases. When two atomically thin crystals are stacked with a slight rotational mismatch, long-wavelength moiré superlattices emerge, reshaping the band structure and vibrational modes through periodic modulation of the local atomic registry. These engineered systems exhibit an extraordinary array of phenomena, including flat-band superconductivity [1–3], gate-tunable ferromagnetism [4], and polar textures akin to ferroelectricity [5–7]. While graphene-based moiré systems have led this revolution, semiconducting transition metal dichalcogenides (TMDs) provide an equally rich landscape, where twist angle, stacking sequence, and layer composition can be precisely controlled to manipulate superconductivity [8,9], correlated insulating states [10–12], moiré excitons [13], phonon modes [14], and charge-density waves [15]. As such, twisted bilayer TMDs have rapidly become a model system for probing and designing emergent quantum states.

At the heart of these phenomena lies interlayer coupling, a fundamental interaction that dictates how stacked layers hybridize electronically, reconstruct structurally, and couple to external stimuli. Interlayer hybridization underpins the formation of flat bands [1,2,10], out-of-plane polarization couples with in-plane shear to enable sliding ferroelectricity [5–7], and excitonic properties can be tuned by controlling the interlayer distance to favor intralayer or interlayer excitons [16]. These diverse examples highlight the critical role of the interlayer distance profile, which defines the spatial landscape of interlayer interactions across the moiré unit cell. Despite its importance, direct access to this structural degree of freedom remains limited. While in-plane reconstructions such as AB/BA domain formation [see Fig. 1(a,b)] have been extensively imaged using piezoresponse force microscopy, scanning tunneling microscope (STM), and transmission electron microscope (TEM), quantitative measurements of out-of-plane (stacking-direction) structure have proven exceptionally challenging. Atomic force microscopy and theoretical modeling suggest interlayer spacing variations of \sim 0.1–0.8 Å across the moiré superlattice [17–23], but three-dimensional reconstruction of interlayer geometry remains elusive, posing a significant barrier to understanding and engineering moiré-driven phenomena.

In principle, diffraction measurements provide a route to extracting three-dimensional (3D) structural information from two-dimensional (2D) materials, just as in conventional crystals. As an illustrative example, Fig. 1c shows a dark-field TEM image of the 0 2 diffraction from twisted bilayer WSe₂ (with 0.3 deg twist angle), revealing triangular AB/BA domains via intensity contrast. This contrast arises from the scattering-vector [$\mathbf{q} = (q_x, q_y, q_z)$] dependence of the diffraction intensity $S(\mathbf{q})$, which differs between AB and BA stacking due to their opposing rod-like scattering features along q_z . The q_z -resolved intensity encodes structural parameters such as the selenium height (h) and interlayer spacing (d), offering a pathway to quantify the out-of-plane structure from tilt-dependent diffraction patterns. However, conventional x-ray diffraction is not viable for atomically thin micro-flake samples. While positron diffraction has succeeded in millimeter-scale bilayer graphene [24], its applicability remains limited for micro-flakes as well. In contrast, TEM offers a compelling solution. Recent advances in automated 3D electron diffraction tomography enable high-precision refinement of structural models [25,26]. Similar principles can be extended to atomically thin materials using tilt-dependent dark-field imaging [27], and further integrated with ultrafast TEM to resolve structural dynamics on picosecond timescales. These emerging techniques provide a powerful foundation for probing the elusive three-dimensional interlayer structure and its dynamics in 2D materials.

In this study, we introduce a method we term “automated dark-field tomography”, which enables quantitative reconstruction of the three-dimensional structure of twisted bilayer systems from tilt-series dark-field TEM images. Using this approach, we directly determine the interlayer spacing and chalcogen atom height in both twisted and naturally stacked bilayer WSe₂, revealing that both are significantly expanded compared to the bulk 2H-WSe₂ phase. Strikingly, we find that twisted bilayer WSe₂ exhibits sub-ångström interlayer decoupling upon heating, an effect absent in naturally stacked counterparts. Moreover, by integrating ultrafast TEM techniques [28,29], we uncover a light-induced, nonthermal expansion of the interlayer spacing on the picosecond timescale, with magnitudes exceeding those in bulk materials. These results establish a powerful new methodology for

structural analysis of 2D materials and reveal the exceptional fragility and tunability of interlayer coupling in twisted bilayers, driven by both thermal and optical stimuli.

Automated dark-field tomography in bilayer WSe₂

To begin with, we discuss the relationship between the dark-field image and the crystal structure of twisted- and natural-bilayer WSe₂. Figure 1(c) shows 0 2 dark-field images of the 0.3° twisted-bilayer WSe₂ at the sample tilt $\alpha = 10^\circ, 18^\circ$, and 24° [see Fig. 1(d) and Sec. 1 in Supplemental Materials]. Characteristic triangular patterns are observed in the dark-field images, where the dark/bright contrast changes as α is varied. This contrast arises from the AB and BA stacking domains realized by the reconstruction of the moiré superlattice in small-angle twisted-bilayer TMDs [30], which can be understood as follows. Figures 1(e,f) show the crystal structure and kinematically simulated dark-field intensity profile $I_{02(0\bar{2})}(\mathbf{q})$ of AB and BA stacking bilayer WSe₂ as a function of \mathbf{q} (see Sec. 1 in Supplemental Materials). Finite-size along the out-of-plane (z) direction in the twisted-bilayer system results in the rod-like $I_{02(0\bar{2})}(\mathbf{q})$ along q_z direction. The dashed white line denotes the cross-section of the Ewald sphere, and the angle θ monotonically changes when the sample tilt α is changed. Therefore, the q_z dependence of $I_{02(0\bar{2})}(\mathbf{q})$ can be obtained via the α -dependent dark-field intensities. The triangular contrast in Fig. 1(c) corresponds to the difference of $I_{02}(q_z)$ in AB/BA stacking domains. Furthermore, the analytical expression of $I_{02}(q_z)$ contains the full atomic coordinates of AB/BA stacking WSe₂, thus we can quantitatively determine the 3D crystal structure parameters from automatically collected α -dependent dark-field image intensity $I_{02}(\mathbf{q})$ (see Sec. 1 in Supplemental Materials]. This method, which we refer to as automated dark-field tomography, can be used for atomically thin flake samples in general. Natural-bilayer 2H-WSe₂ also shows rod-like $I_{02}(\mathbf{q})$ [Figs. 1(g,h)] with q_z dependence significantly different from AB/BA stacking. Thus the crystal structure parameters of natural-bilayer 2H-WSe₂ can also be determined from automated dark-field tomography.

Crystal structure refinement of twisted- and natural-bilayer WSe₂

Here, we experimentally determine the interlayer distance of twisted- and natural-bilayer WSe₂ using automated dark-field tomography. Figure 2(a) shows the dark-field intensity $I_{02}(\alpha)$ curves taken within the AB/BA stacking domains, as marked by the blue/red rectangles in the inset image. We fitted them by the squared structure factor $|S_{02}(\alpha, d_{\text{TBL}}, h_{\text{TBL}})|^2$ to determine d_{TBL} and h_{TBL} [see Sec. 1 in Supplemental Materials for detail]. We assumed that the selenium height h_{TBL} is identical for all selenium atoms for simplicity. The solid gray curves in Fig. 2(a) are the fitting results that most well reproduce the experimental data. Here we obtained the structural parameters as $d_{\text{TBL}} = 6.64 \pm 0.10 \text{ \AA}$ and $h_{\text{TBL}} = 1.76 \pm 0.10 \text{ \AA}$. We also measured the natural-bilayer 2H-WSe₂, as shown in the inset in Fig. 2(b). Similarly to the twisted-bilayer sample, $I_{02}(\alpha)$ of the bilayer 2H-WSe₂ was taken at the blue rectangle region (inset) and fitted by the gray solid curve. d_{2H} and h_{2H} are obtained as $6.63 \pm 0.10 \text{ \AA}$ and $1.77 \pm 0.10 \text{ \AA}$, respectively.

The results of crystal structure refinements for twisted- and natural- bilayer WSe₂ are summarized in Fig. 2(c), along with the literature values for bulk 2H-WSe₂ [31]. The results of structural relaxation from density-functional theory (DFT) calculations are also plotted by filled markers (see methods). Compared with bulk 2H-WSe₂, both twisted- and natural-bilayer WSe₂ show significantly large interlayer distance d , although the selenium height h is seemingly scattered within the experimental error. The larger interlayer distance observed in both bilayer systems suggests a reduced interlayer coupling, which should significantly affect their electronic and optical properties, as discussed later. The DFT calculation results (filled markers) also show the significant difference between the interlayer distance of bulk and bilayer samples, well reproducing the experimental results. This result gives the validation of the DFT calculations in twisted-bilayer systems, at least in the relaxed AB/BA regions.

Thermally-induced sub-Å interlayer decoupling

We further perform the temperature-dependent automated dark-field tomography of natural- and twisted- bilayer-WSe₂, and reveal the thermally induced sub-Å interlayer decoupling in the twisted-bilayer sample. Fig. 2(d) shows the temperature-dependent $I_{02}(\alpha)$ curves for $24 < \alpha < 35$, taken at the BA stacking region. At 400 K, the peak position is slightly shifted towards the lower α direction compared to 300 K. On the other hand, $I_{02}(\alpha)$ for the natural-bilayer sample [Fig. 2(e)] does not show any significant shift. Similar behaviors were also observed in the AB stacking counterpart and other α region [Sec. 2 in Supplemental Materials]. Correspondingly, the fitting results of the twisted-bilayer sample show the change in the interlayer distance $\Delta d_{\text{TBL}} = d_{\text{TBL}}(T = 400 \text{ K}) - d_{\text{TBL}}(T = 300 \text{ K})$ of 0.08 Å [Fig. 2(f)], whereas no significant change is observed in the natural-bilayer sample [Fig. 2(g)]. The estimated linear thermal expansion coefficient along z for the twisted-bilayer sample is $\beta = 8.0 \times 10^{-5} \text{ K}^{-1}$, which is much larger than those of the natural-bilayer sample ($< 2.0 \times 10^{-5} \text{ K}^{-1}$) and the bulk 2H-WSe₂ sample [32] ($1.0 \times 10^{-5} \text{ K}^{-1}$) as summarized in Fig. 2(h). This value is comparable to polymers such as polyvinyl chloride, showing larger thermal expansion compared to inorganic solids [33]. These results prove the thermally induced sub-Å interlayer decoupling unique to the *twisted*-bilayer system.

This anomalously large thermal expansion and sub-Å interlayer decoupling observed exclusively in the twisted-bilayer sample may originate from its unique bonding configuration associated with the catenary-like interlayer state. In twisted bilayers, the interlayer coupling is highly nonuniform across the moiré superlattice: theoretical studies [23,21,18] have predicted a substantial difference in the interlayer spacing between the AA stacking regions, where the layers are maximally separated at the vertices of the triangular pattern, and the AB/BA stacking regions, where the layers are most closely spaced, with a magnitude on the order of several tenths of an ångström. Recent STM study also reveals the out-of-plane atomic reconstruction depending on the stacking [34]. The present results, obtained from the structurally relaxed AB/BA regions, already indicate an unusually strong anharmonicity in the interlayer bonding potential of the twisted-bilayer system. Such enhanced anharmonicity may naturally lead to a large out-of-plane thermal response, far exceeding that of natural bilayers and bulk crystals. Although the current measurements are

limited to the AB/BA domains, further improvement of spatial resolution will enable direct access to the AA regions and the ridge-like domain boundaries of the moiré lattice. Probing these local structures is expected to provide decisive insights into the microscopic mechanism underlying the thermally induced interlayer decoupling in twisted bilayer WSe₂.

Non-thermal interlayer decoupling induced by pulsed light

We further investigate the photoinduced structural dynamics of twisted-bilayer WSe₂ (Sample #2) using ultrafast TEM [Fig. 3(a)]. Sample #2 is characterized in Sec. 3 in Supplemental Materials. Figure 3(b) shows the 0 2 dark-field image $I_{02}(t)$ of twisted-bilayer WSe₂ before photoexcitation, where triangular patterns are observed. Although these reconstructed AB/BA stacking domains in Fig. 3(b) were stable under equilibrium conditions for more than a month, they change abruptly and irreversibly when the sample is continuously photoexcited by a sequence of 25 kHz 2.4 eV light pulses for several days [see Fig. 3(c) and Sec. 3 in Supplemental Materials]. The AB/BA domains at the center of the image lose the ordered triangular shape, but after one week, the structural AB/BA domain shown in Fig. 3(c) was stable.

Here, we investigate the crystal structure dynamics of WSe₂ from the time-dependent change in dark-field image intensity. Figure 3(d) shows the 0 2 dark-field image of twisted-bilayer WSe₂ measured at $\alpha = 24.1^\circ$. When the 2.4 eV light pulse of 0.33 mJ/cm^2 excites the sample, the dark-field-image intensity in the AB (BA) stacking region decreases (increases), as shown in Figs. 3(e,f). We found that triangular AB/BA domains also show a similar trend, as in Extended Data Fig. 1, suggesting that the observed domain-dependent change in dark-field images is universal regardless of the domain shape. To quantitatively analyze the dark-field intensity, we subtracted the background and obtained the normalized dark-field intensity $\bar{I}_{02}(t)$ for AB/BA domains as shown in Fig. 3(g) (see Sec. 4 in Supplemental Materials for details). $\bar{I}_{02}(t)$ of the AB (BA) domain decreases (increases) immediately after the photoexcitation, within the time resolution 4 ps, and then relaxes back.

From the transient dark field intensity change, we further evaluate the time dependence of the interlayer distance $d_{\text{TBL}}(t)$, revealing a sub-Å change in the interlayer distance. By comparing $I_{02}(t)$ and the simulated crystal structure factor $|S_{02}(\alpha, d_{\text{TBL}}, h_{\text{TBL}})|^2$ quantitatively, we can determine $d_{\text{TBL}}(t)$. For BA stacking, the effect of $h_{\text{TBL}}(t)$ on $I_{02}(t)$ is negligible, and we can only evaluate $d_{\text{TBL}}(t)$ (see Sec. 4 in Supplemental Material). As shown in Fig. 4(a), the obtained $\Delta d_{\text{TBL}}(t) = d_{\text{TBL}}(t) - d_{\text{TBL}}(t < 0)$ increases by 0.2 Å at $t \sim 0$ and subsequently relaxes. Regarding the AB stacking, on the other hand, h_{TBL} and d_{TBL} both contribute to $I_{02}(t)$ and they cannot be independently evaluated. Here we adopt $\Delta h_{\text{TBL}}(t) = h_{\text{TBL}}(t) - h_{\text{TBL}}(t < 0) = 0$, which provides the solution of $\Delta d_{\text{TBL}}(t)$ similar to the BA stacking (see Sec. 4 in Supplemental Material).

As shown in Fig. 4(a), in the relaxation process, Δd_{TBL} apparently shows the fast (about 50 ps) and slow (> 200 ps) relaxation components. To discuss the origin of these relaxation components, we evaluated the change in the transient lattice temperature ΔT from the Debye-Waller factor of 4 0 diffraction intensity, which is further normalized by that just after the photo-excitation (ΔT_{max}) (see Sec. 5 in Supplemental Materials). The $\Delta T/\Delta T_{\text{max}}$ curve in Fig. 4(b) behaves differently from Δd_{TBL} : an exponential decay curve with a single time constant of 200 ps can well describe $\Delta T/\Delta T_{\text{max}}$ curve between 0 and 400 ps. These results indicate that the photoinduced change in the interlayer distance cannot be attributed to the change in the transient lattice temperature and should be non-thermal, at least in the fast (< 50 ps) timescale.

The appearance of fast and slow decay components in the interlayer distance is reminiscent of exciton dynamics observed in monolayer samples [35–38]. When the exciton density is sufficiently high in these systems, relatively fast (< 100 ps) decay of excitons due to the exciton-exciton annihilation process has been reported in addition to the slow (100 ps \sim few ns) recombination process. Such an exciton-exciton annihilation process is not observed in bulk and, therefore, is unique to atomically thin samples [37]. These previous studies indicate that the non-thermal interlayer decoupling observed in Fig. 4(a) may be attributed to the positive stress due to the exciton generation that is located at around 1.5–1.7 eV in twisted-bilayer WSe₂ [39]. The stress caused by the semiconductor carriers, including

excitons, is usually described by deformation potential, which is related to the pressure-dependent electronic band structure [40]. Considering that the hydrostatic pressure significantly affects the interlayer coupling and bandgap in the bilayer system [41], the deformation potential mechanism caused by the exciton is a plausible scenario for the change in the interlayer distance. In addition, we also mention that the Δd_{TBL} at 400 ps [Fig. 4(a)] is not fully relaxed to the initial state while $\Delta T/\Delta T_{\text{max}}$ is almost zero [Fig. 4(b)]. This indicates the relatively slow ($t > 400$ ps) exciton recombination process, in addition to the fast exciton-exciton annihilation (< 50 ps) and thermal relaxation (~ 200 ps) as summarized in Fig. 4(c).

The observed 0.2 Å change in interlayer distance is significantly larger as compared to previous studies on various bulk materials [41,42]. In bulk graphite [41], the magnitude of the change in interlayer distance is less than 0.01 Å even at a pump fluence of 11 mJ/cm², a value significantly different from the present result (0.2 Å at 0.33 mJ/cm²). $\Delta d_{\text{TBL}} = 0.2$ Å is comparable to the 25-50% interlayer distance variation between AA and AB/BA stacking predicted by the theoretical calculations [23,21,18]. Although we do not observe any reversible change in the AB/BA stacking domain shape on the picosecond scale, frequent repetition of such a giant change in the interlayer distance may induce the deformation of the local twist angle and the resultant disordered domain structures, as seen in Fig. 3(b,c). Such a photoinduced domain reconstruction should be further investigated in future studies.

Discussion: Impact of sub-Å interlayer decoupling

The observed thermally and optically induced sub-Å interlayer decoupling will significantly impact various properties of twisted materials. The previous experiments reported that the properties of twisted-bilayer systems are significantly modified via a change in the interlayer distance, e.g., tuning of superconductivity [43], change in the indirect bandgap [18], formation of commensurate stacking [44], and modification of the electronic van Hove singularities [22]. In addition, many theoretical calculations [18,17,19,22,45,46] have revealed the band structure modification due to the change in the interlayer distance because it can directly affect the interlayer coupling. Based on the theoretical calculation in

Ref. [18], $\Delta d_{\text{TBL}} = 0.2 \text{ \AA}$ changes the indirect bandgap of MoS₂ by about 100 meV, although the direct bandgap at the K point is not significantly modified [18]. Such a large modification of the bandgap may induce direct-indirect bandgap transition in twisted-bilayer TMD semiconductors. Therefore, the thermally and optically induced sub- \AA interlayer decoupling revealed by the present work should be essential in interpreting future research on twisted-bilayer systems. In particular, an interlayer decoupling effect caused by the excitons should play an essential role in the optical nature of the twisted-bilayer system.

Conclusions

In conclusion, we investigated the thermally and optically induced interlayer decoupling in twisted-bilayer WSe₂ using TEM. A newly developed automated dark-field tomography enables us to quantitatively determine the three-dimensional crystal structure of twisted- and natural-bilayer WSe₂. It reveals that both twisted- and natural-bilayer samples show interlayer decoupling by 0.15 \AA compared to bulk samples. Additional thermally-induced interlayer decoupling is also observed only in the twisted-bilayer sample, which is significantly larger than the bulk and natural-bilayer samples. Further investigation of picosecond crystal structure dynamics after photoexcitation revealed a non-thermal interlayer decoupling reaching 0.2 \AA , probably due to the exciton generation. Such sub- \AA interlayer decoupling in equilibrium and non-equilibrium states should significantly impact the electronic and optical properties of twisted-bilayer materials, and should be carefully considered in future studies. Application of the TEM-based methods presented in this study to a variety of materials/phenomena, such as sliding ferroelectricity [5–7], moiré enhanced charge-density wave [15], and light-induced ferromagnetism [47], is a promising direction in the future.

References

- [1] Y. Cao, V. Fatemi, S. Fang, K. Watanabe, T. Taniguchi, E. Kaxiras, and P. Jarillo-Herrero, Unconventional superconductivity in magic-angle graphene superlattices, *Nature* **556**, 7699 (2018).
- [2] X. Lu et al., Superconductors, orbital magnets and correlated states in magic-angle bilayer graphene, *Nature* **574**, 7780 (2019).
- [3] R. Bistritzer and A. H. MacDonald, Moiré bands in twisted double-layer graphene, *Proceedings of the National Academy of Sciences* **108**, 12233 (2011).
- [4] A. L. Sharpe, E. J. Fox, A. W. Barnard, J. Finney, K. Watanabe, T. Taniguchi, M. A. Kastner, and D. Goldhaber-Gordon, Emergent ferromagnetism near three-quarters filling in twisted bilayer graphene, *Science* **365**, 605 (2019).
- [5] Z. Zheng et al., Unconventional ferroelectricity in moiré heterostructures, *Nature* **588**, 7836 (2020).
- [6] M. Vizner Stern, Y. Waschitz, W. Cao, I. Nevo, K. Watanabe, T. Taniguchi, E. Sela, M. Urbakh, O. Hod, and M. Ben Shalom, Interfacial ferroelectricity by van der Waals sliding, *Science* **372**, 1462 (2021).
- [7] K. Yasuda, X. Wang, K. Watanabe, T. Taniguchi, and P. Jarillo-Herrero, Stacking-engineered ferroelectricity in bilayer boron nitride, *Science* **372**, 1458 (2021).
- [8] Y. Xia, Z. Han, K. Watanabe, T. Taniguchi, J. Shan, and K. F. Mak, Superconductivity in twisted bilayer WSe₂, *Nature* **637**, 833 (2025).
- [9] Y. Guo et al., Superconductivity in 5.0° twisted bilayer WSe₂, *Nature* **637**, 839 (2025).
- [10] L. Wang et al., Correlated electronic phases in twisted bilayer transition metal dichalcogenides, *Nat. Mater.* **19**, 8 (2020).
- [11] Y. Tang et al., Simulation of Hubbard model physics in WSe₂/WS₂ moiré superlattices, *Nature* **579**, 7799 (2020).
- [12] Y. Xu, S. Liu, D. A. Rhodes, K. Watanabe, T. Taniguchi, J. Hone, V. Elser, K. F. Mak, and J. Shan, Correlated insulating states at fractional fillings of moiré superlattices, *Nature* **587**, 7833 (2020).
- [13] D. Huang, J. Choi, C.-K. Shih, and X. Li, Excitons in semiconductor moiré superlattices, *Nat. Nanotechnol.* **17**, 3 (2022).
- [14] J. Quan et al., Phonon renormalization in reconstructed MoS₂ moiré superlattices, *Nat. Mater.* **20**, 8 (2021).
- [15] W.-M. Zhao, L. Zhu, Z. Nie, Q.-Y. Li, Q.-W. Wang, L.-G. Dou, J.-G. Hu, L. Xian, S. Meng, and S.-C. Li, Moiré enhanced charge density wave state in twisted 1T-TiTe₂/1T-TiSe₂ heterostructures, *Nat. Mater.* **21**, 3 (2022).
- [16] X. Ma, S. Fu, J. Ding, M. Liu, A. Bian, F. Hong, J. Sun, X. Zhang, X. Yu, and D. He, Robust Interlayer Exciton in WS₂ /MoSe₂ van der Waals Heterostructure under High Pressure, *Nano Lett.* **21**, 8035 (2021).
- [17] I. Brihuega, P. Mallet, H. González-Herrero, G. Trambly de Laissardière, M. M. Ugeda, L. Magaud, J. M. Gómez-Rodríguez, F. Ynduráin, and J.-Y. Veuillen, Unraveling the Intrinsic and Robust Nature of van Hove Singularities in Twisted Bilayer Graphene by Scanning Tunneling Microscopy and Theoretical Analysis, *Phys. Rev. Lett.* **109**, 196802 (2012).
- [18] K. Liu, L. Zhang, T. Cao, C. Jin, D. Qiu, Q. Zhou, A. Zettl, P. Yang, S. G. Louie, and F. Wang, Evolution of interlayer coupling in twisted molybdenum disulfide bilayers, *Nat Commun* **5**, 1 (2014).
- [19] E. Del Corro et al., Fine tuning of optical transition energy of twisted bilayer graphene via interlayer distance modulation, *Phys. Rev. B* **95**, 085138 (2017).
- [20] B. L. Chittari, N. Leconte, S. Javvaji, and J. Jung, Pressure induced compression of flatbands in twisted bilayer graphene, *Electron. Struct.* **1**, 015001 (2018).
- [21] A. Weston et al., Atomic reconstruction in twisted bilayers of transition metal dichalcogenides, *Nat. Nanotechnol.* **15**, 7 (2020).
- [22] Y.-X. Zhao, X.-F. Zhou, Y. Zhang, and L. He, Oscillations of the Spacing between van Hove Singularities Induced by sub-ÅAA {ngstrom Fluctuations of Interlayer Spacing in Graphene Superlattices, *Phys. Rev. Lett.* **127**, 266801 (2021).
- [23] T. Devakul, V. Crépel, Y. Zhang, and L. Fu, Magic in twisted transition metal dichalcogenide bilayers, *Nat Commun* **12**, 1 (2021).

- [24] Y. Fukaya, Y. Zhao, H.-W. Kim, J. R. Ahn, H. Fukidome, and I. Matsuda, Atomic arrangements of quasicrystal bilayer graphene: Interlayer distance expansion, *Phys. Rev. B* **104**, L180202 (2021).
- [25] L. Palatinus, P. Brázda, P. Boullay, O. Perez, M. Klementová, S. Petit, V. Eigner, M. Zaarour, and S. Mintova, Hydrogen positions in single nanocrystals revealed by electron diffraction, *Science* **355**, 166 (2017).
- [26] P. B. Klar, Y. Krysiak, H. Xu, G. Steciuk, J. Cho, X. Zou, and L. Palatinus, Accurate structure models and absolute configuration determination using dynamical effects in continuous-rotation 3D electron diffraction data, *Nat. Chem.* **15**, 848 (2023).
- [27] S. H. Sung, N. Schnitzer, L. Brown, J. Park, and R. Hovden, Stacking, strain, and twist in 2D materials quantified by 3D electron diffraction, *Phys. Rev. Materials* **3**, 064003 (2019).
- [28] A. Nakamura, T. Shimojima, Y. Chiashi, M. Kamitani, H. Sakai, S. Ishiwata, H. Li, and K. Ishizaka, Nanoscale Imaging of Unusual Photoacoustic Waves in Thin Flake VTe 2, *Nano Letters* **20**, 4932 (2020).
- [29] T. Shimojima, A. Nakamura, and K. Ishizaka, Development of five-dimensional scanning transmission electron microscopy, *Review of Scientific Instruments* **94**, 023705 (2023).
- [30] L. Brown, R. Hovden, P. Huang, M. Wojcik, D. A. Muller, and J. Park, Twinning and Twisting of Tri- and Bilayer Graphene, *Nano Letters* **12**, 1609 (2012).
- [31] W. J. Schutte, J. L. De Boer, and F. Jellinek, Crystal structures of tungsten disulfide and diselenide, *Journal of Solid State Chemistry* **70**, 207 (1987).
- [32] S. H. El-Mahalawy and B. L. Evans, The thermal expansion of 2H-MoS2, 2H-MoSe2 and 2H-WSe2 between 20 and 800°C, *J Appl Cryst* **9**, 5 (1976).
- [33] M. Titow, *PVC Technology* (Springer Science & Business Media, 2012).
- [34] H. Zhao, S. Yang, C. Ge, D. Zhang, L. Huang, M. Chen, A. Pan, and X. Wang, Tunable Out-of-Plane Reconstructions in Moiré Superlattices of Transition Metal Dichalcogenide Heterobilayers, *ACS Nano* **18**, 27479 (2024).
- [35] D. Sun, Y. Rao, G. A. Reider, G. Chen, Y. You, L. Brézin, A. R. Harutyunyan, and T. F. Heinz, Observation of Rapid Exciton–Exciton Annihilation in Monolayer Molybdenum Disulfide, *Nano Lett.* **14**, 5625 (2014).
- [36] S. Mouri, Y. Miyauchi, M. Toh, W. Zhao, G. Eda, and K. Matsuda, Nonlinear photoluminescence in atomically thin layered WSe 2 arising from diffusion-assisted exciton-exciton annihilation, *Phys. Rev. B* **90**, 155449 (2014).
- [37] N. Kumar, Q. Cui, F. Ceballos, D. He, Y. Wang, and H. Zhao, Exciton-exciton annihilation in MoSe 2 monolayers, *Phys. Rev. B* **89**, 125427 (2014).
- [38] M. Kulig, J. Zipfel, P. Nagler, S. Blanter, C. Schüller, T. Korn, N. Paradiso, M. M. Glazov, and A. Chernikov, Exciton Diffusion and Halo Effects in Monolayer Semiconductors, *Phys. Rev. Lett.* **120**, 207401 (2018).
- [39] T. I. Andersen et al., Excitons in a reconstructed moiré potential in twisted WSe2/WSe2 homobilayers, *Nat. Mater.* **20**, 480 (2021).
- [40] P. Ruello and V. E. Gusev, Physical mechanisms of coherent acoustic phonons generation by ultrafast laser action, *Ultrasonics* **56**, 21 (2015).
- [41] F. Carbone, P. Baum, P. Rudolf, and A. H. Zewail, Structural Preablation Dynamics of Graphite Observed by Ultrafast Electron Crystallography, *Phys. Rev. Lett.* **100**, 035501 (2008).
- [42] T. Suzuki et al., Ultrafast optical stress on $\{ \text{BaFe} \}_{2} \{ \text{As} \}_{2}$, *Phys. Rev. Research* **3**, 033222 (2021).
- [43] M. Yankowitz, S. Chen, H. Polshyn, Y. Zhang, K. Watanabe, T. Taniguchi, D. Graf, A. F. Young, and C. R. Dean, Tuning superconductivity in twisted bilayer graphene, *Science* **363**, 1059 (2019).
- [44] M. Yankowitz, K. Watanabe, T. Taniguchi, P. San-Jose, and B. J. LeRoy, Pressure-induced commensurate stacking of graphene on boron nitride, *Nat Commun* **7**, 13168 (2016).
- [45] S. Carr, S. Fang, P. Jarillo-Herrero, and E. Kaxiras, Pressure dependence of the magic twist angle in graphene superlattices, *Phys. Rev. B* **98**, 085144 (2018).
- [46] M. Romanova and V. Vlček, Stochastic many-body calculations of moiré states in twisted bilayer graphene at high pressures, *Npj Comput Mater* **8**, 11 (2022).

- [47] X. Wang et al., Light-induced ferromagnetism in moiré superlattices, *Nature* **604**, 468 (2022).
- [48] S. Masubuchi, M. Morimoto, S. Morikawa, M. Onodera, Y. Asakawa, K. Watanabe, T. Taniguchi, and T. Machida, Autonomous robotic searching and assembly of two-dimensional crystals to build van der Waals superlattices, *Nat Commun* **9**, 1 (2018).
- [49] K. Kim et al., van der Waals Heterostructures with High Accuracy Rotational Alignment, *Nano Lett.* **16**, 1989 (2016).
- [50] A. Nakamura, lys: interactive multi-dimensional data analysis and visualization platform, *Journal of Open Source Software* **8**, 5869 (2023).
- [51] G. Kresse and J. Hafner, Ab initio molecular dynamics for liquid metals, *Physical Review B* **47**, 558 (1993).
- [52] S. Grimme, J. Antony, S. Ehrlich, and H. Krieg, A consistent and accurate *ab initio* parametrization of density functional dispersion correction (DFT-D) for the 94 elements H-Pu, *The Journal of Chemical Physics* **132**, 154104 (2010).
- [53] C. Riekel, Structure refinement of TiSe₂ by neutron diffraction, *Journal of Solid State Chemistry* **17**, 389 (1976).
- [54] F. A. Cevallos et al., Liquid Salt Transport Growth of Single Crystals of the Layered Dichalcogenides MoS₂ and WS₂, *Crystal Growth & Design* **19**, 5762 (2019).
- [55] K. D. Bronsema, G. W. Bus, and G. A. Wiegers, The crystal structure of vanadium ditelluride, V_{1+x}Te₂, *Journal of Solid State Chemistry* **53**, 415 (1984).
- [56] B. E. Brown, The crystal structures of NbT₂ and TaTe₂, *Acta Cryst* **20**, 264 (1966).
- [57] B. E. Brown, The crystal structures of WTe₂ and high-temperature MoTe₂, *Acta Crystallographica* **20**, 268 (1966).
- [58] A. Spijkerman, J. L. de Boer, A. Meetsma, G. A. Wiegers, and S. van Smaalen, X-ray crystal-structure refinement of the nearly commensurate phase of 1 T – TaS₂ in (3 + 2) -dimensional superspace, *Phys. Rev. B* **56**, 13757 (1997).
- [59] T. Sörgel, J. Nuss, U. Wedig, R. K. Kremer, and M. Jansen, A new low temperature modification of TaTe₂—Comparison to the room temperature and the hypothetical 1T-TaTe₂ modification, *Materials Research Bulletin* **41**, 987 (2006).

Acknowledgments:

This work was supported by JSPS KAKENHI (Grant numbers 25K00057, JP20H01834, JP21H05235, JP24K01285, 24H00410, JP25H01251), JST PRESTO (Grant number JPMJPR24JA), CREST (Grant number. JPMJCR20B4). T. S. acknowledges support from Toray Science Foundation (#23-6405)、The Sumitomo Foundation. K.W. and T.T. acknowledge support from the JSPS KAKENHI (Grant numbers 21H05233 and 23H02052), JST CREST (JPMJCR24A5), and World Premier International Research Center Initiative (WPI), MEXT, Japan.

Methods

Setup of (ultrafast) transmission electron microscopy

Transmission electron microscopy measurements were performed using a previously described system [28] based on Tecnai Femto (Thermo Fisher Scientific). The 150- μm condenser aperture was used for all measurements. We used a 20- μm objective aperture for bright-field and dark-field measurements unless otherwise denoted. A selected-area aperture of 200 μm was used for the diffraction measurements. For the automated dark-field tomography measurements, sample-tilt-dependent dark-field images are automatically collected with an angle step of 0.5°. For the time-resolved measurements in Fig. 4, we use 1030-nm light source PHAROS (Light Convergion) with the repetition rate of 25 kHz. We used frequency-doubled 514-nm light with a fluence of 330 $\mu\text{J}/\text{cm}^2$ as the pump light. The total time resolution was set at 4 ps for data acquisition to maintain a good signal-to-noise ratio throughout the entire measurement, although the best time resolution of our ultrafast transmission electron microscopy system was 750 fs. The spatial resolution of all measurements is less than 20 nm. The beam diameter of the pump light (\sim 160 μm) was set much larger than that of the sample ($< 10 \mu\text{m}$).

Sample preparation

The twisted-bilayer WSe₂ and few-layer 2H-WSe₂ samples were fabricated by the mechanical exfoliation of bulk 2H-WSe₂ (2D Semiconductors) and dry-transfer method using Elvacite 2552C (Lucite International Inc.) as a polymer stamp. method described in Ref. [48]. The twist angles were set to 0.3° by tear-and-stack method [49], although the actual twist angle slightly varies around this value depending on the position. The WSe₂ flakes were sandwiched between a few layers of hexagonal boron nitride (hBN) and then placed on an amorphous silicon nitride (SiN_x) substrate (Norcada Inc.). We prepared two twisted-bilayer WSe₂ samples (Sample #1 and #2), which are used for temperature-dependent and time-resolved measurements, respectively. We use 20-nm and 100-nm SiN_x substrate for Sample #1 and #2, respectively.

Drift correction of time-dependent data

For the time-dependent dark-field image measurement in Fig. 4, we performed time-dependent dark-field image measurements repeatedly, and these data are summed to improve the signal-to-noise ratio. Before the summation, the sample drift between several measurements was corrected. We numerically evaluated the cross-correlation of dark-field images as follows:

$$A_{t,n}(x_i, y_j) = \sum_{p,q=-N/4}^{N/4} I_{t,n}(x_p, y_q) I_{\text{ref}}(x_p - x_i, y_q - y_j),$$

where $I_{t,n}(x_p, y_q)$ is the dark-field image at delay time t of n -th measurement, $I_{\text{ref}}(x_p, y_q)$ is the dark-field image at $t = -100$ ps of the first measurement, $x_{i,p}, y_{j,q}$ represents the pixelated position in the image, $N = 256$ is the image size. Therefore, $A_{t,n}(x_i, y_j)$ is the cross-correlation of the central part of the image. We estimated the shift of the dark-field image as the maximum position of $A_{t,n}(x_i, y_j)$, by which the respective image was shifted. The typical magnitude of the shift was 0-4 pixels. All analyses were done using multi-dimensional data analysis and visualization platform lys [50].

Density-functional calculations

Density-functional theory (DFT) calculations using VASP package [51] were performed to evaluate the structural parameters of AB and 2H stacking bilayer WSe₂ and bulk 2H-WSe₂. It is noted that we do not include the effect of twisted crystal structure for AB stacking bilayer WSe₂. The calculations were performed in the framework of the van der Waals density functional theory [52] using the pseudo-potential method in conjunction with the generalized gradient approximation. The wave functions were expanded in the plane wave basis with the cutoff energy of 500 eV to ensure good convergence of the stress and elastic tensor. The k -point sampling was set to $9 \times 9 \times 4$ in the first Brillouin zone. The a axis length was fixed to 3.32 Å, which is experimentally determined by the electron diffraction measurement. The interlayer distance and selenium height were relaxed with a

force convergence of 0.0015 eV/Å. Although the two selenium heights are relaxed independently, the difference between them are less than 0.001 Å.

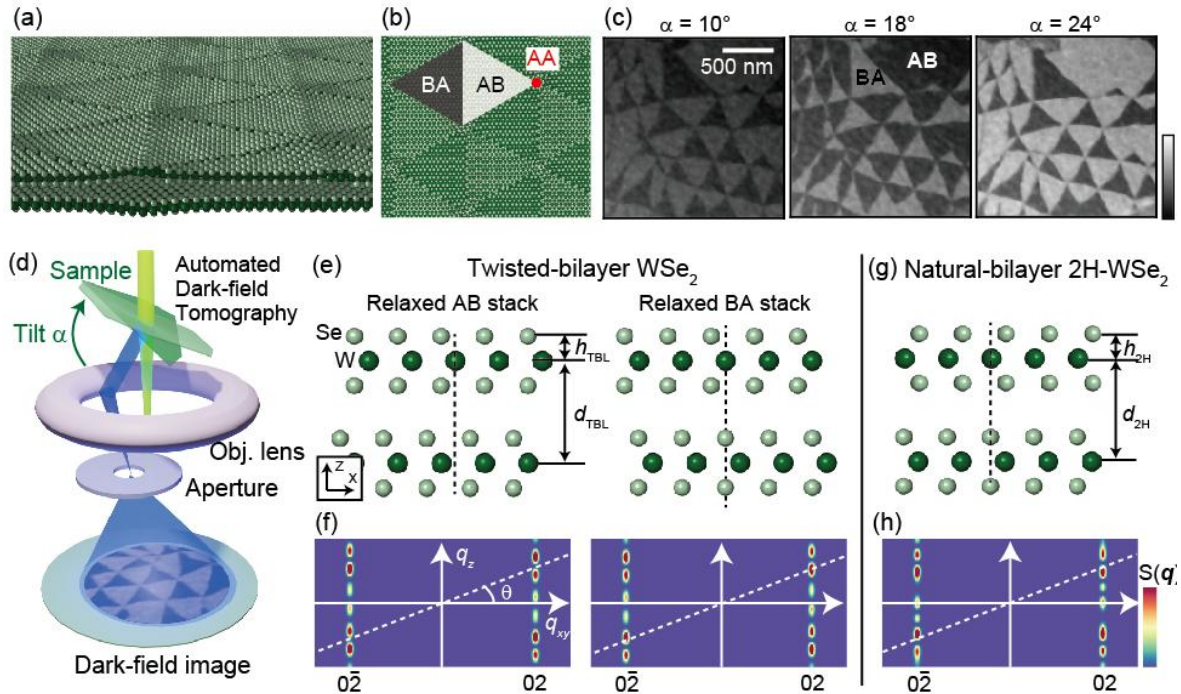


Fig. 1. (a) Schematic of superlattice relaxation in twisted-bilayer WSe₂. Dark- and light-green spheres denote tungsten and selenium atoms, respectively. For clarity, the spatial variation of interlayer distance due to the relaxation is emphasized. (b) Top view of the twisted-bilayer WSe₂. AA, AB, and BA stand for the AA, AB, and BA stacking regions of WSe₂ layers (c) 0 2 dark-field images of twisted-bilayer WSe₂ sample at the sample tilt $\alpha = 10^\circ$, 18° , and 24° , respectively. The triangular contrast reflects the AB/BA stacking domains. (d) Schematic of the automated dark-field tomography. Dark-field images of twisted-bilayer WSe₂ are recorded by changing the sample tilt α . (e) Side view of the twisted-bilayer WSe₂ at relaxed AB and BA stacking regions. d_{TBL} and h_{TBL} denote interlayer distance and selenium height. (f) The calculated diffraction intensity profile for AB, BA stacking bilayer WSe₂, which is squared crystal structure factor $|S(\mathbf{q})|^2$ described in Sec. 1 in Supplemental Materials. The dashed white line denotes the Ewald sphere corresponding to $\alpha = 18^\circ$. (g) Side view of natural-bilayer 2H-WSe₂. d_{2H} and h_{2H} denote interlayer distance and selenium height. (h) The calculated diffraction intensity profile for 2H stacking bilayer WSe₂.

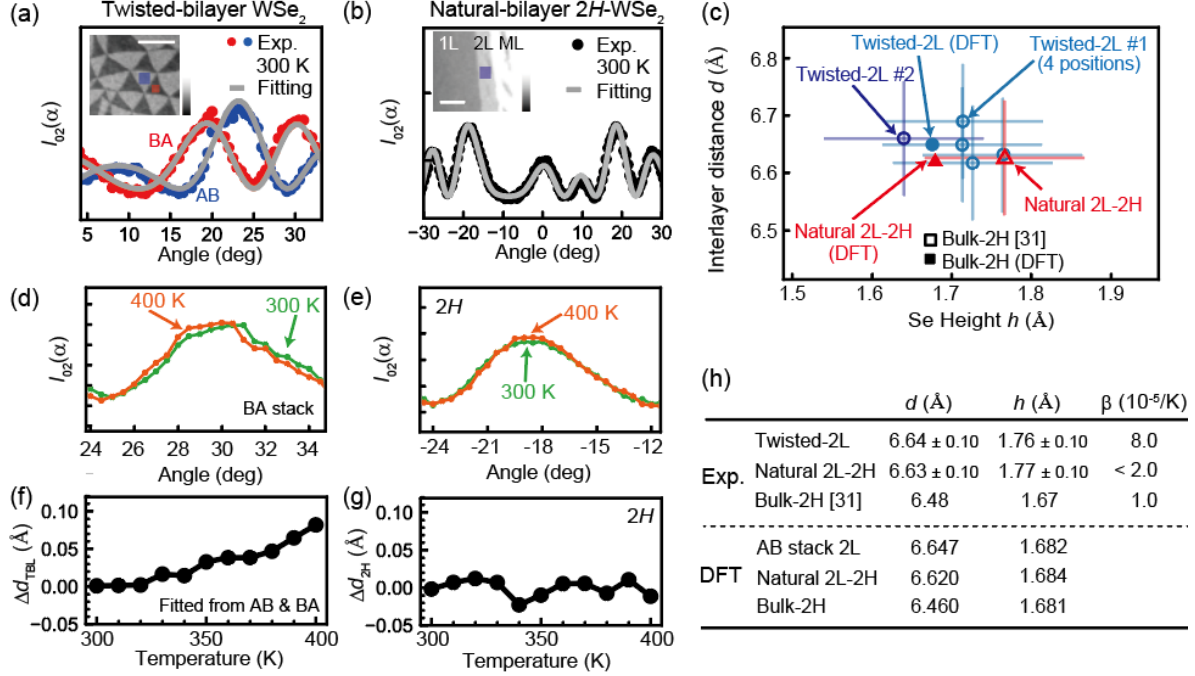


Fig. 2. (a) Automated dark-field tomography data of 0 2 diffraction [$I_{02}(\alpha)$] of AB and BA stacking domains in twisted-bilayer WSe₂. The blue and red regions in the inset show where $I_{02}(\alpha)$ is obtained. The solid gray curves denote fitting results. The white scale bar in the inset denotes 500 nm. The vertical axes of a-d are on a linear scale. (b) $I_{02}(\alpha)$ of natural-bilayer 2H-WSe₂. The blue rectangle in the inset shows where $I_{02}(\alpha)$ is obtained. In the inset, 1L, 2L, and ML indicate monolayer, bilayer, and multilayer WSe₂ obtained from the bulk 2H-WSe₂ by exfoliation. The white scale bar in the inset denotes 500 nm. (c) Interlayer distance (d_{TBL}, d_{2H}) and selenium height (h_{TBL}, h_{2H}) obtained from automated dark-field tomography. Blue open circles denote the result of twisted-bilayer WSe₂, while the red open triangle is that of natural-bilayer 2H-WSe₂. We performed five independent measurements on the twisted-bilayer WSe₂ by changing the sample (#1, #2) and position (4 positions on sample #1) in the sample. The black rectangle is the interlayer distance and selenium height of bulk 2H-WSe₂ in the literature [31]. The filled markers denote the DFT calculation results (see methods). (d,e) Magnified $I_{02}(\alpha)$ curve measured at 300 K and 400 K. (f,g) Temperature dependence of the interlayer distance d_{TBL} and d_{2H} obtained from the fitting (see Sec. 1 in Supplemental Materials). (h) The list of the interlayer distance d , selenium height h , and

linear thermal expansion coefficient β obtained from the automated dark-field tomography and density-functional calculations. For the twisted-bilayer WSe₂, we use the results obtained from a.

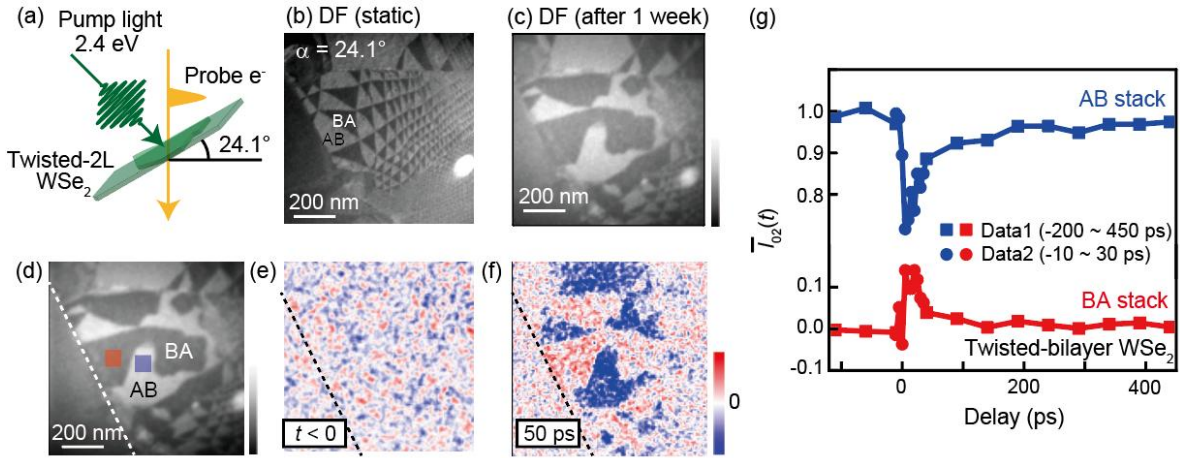


Fig. 3. (a) Schematic of ultrafast TEM measurement on twisted-bilayer WSe₂ (see methods for details). The sample tilt α was fixed to 24.1° . (b,c) 0 2 dark-field images of twisted-bilayer WSe₂ before and one week after continuous photoexcitation by a 2.4 eV light pulses. The bright and dark regions denote AB and BA stacking domains, respectively. (d) The 0 2 dark-field image of twisted-bilayer WSe₂ before photoexcitation ($t < 0$). There is a monolayer region at the bottom-left region, denoted by the white dashed line. (e,f) Change in 0 2 dark-field images $I_{02}(t) - I_{02}(t < 0)$ before and after photoexcitation. (g) A background-subtracted normalized dark-field image intensity $\bar{I}_{02}(t)$ at the blue and red rectangles in d (see Sec. 4 in Supplemental Materials for detail).

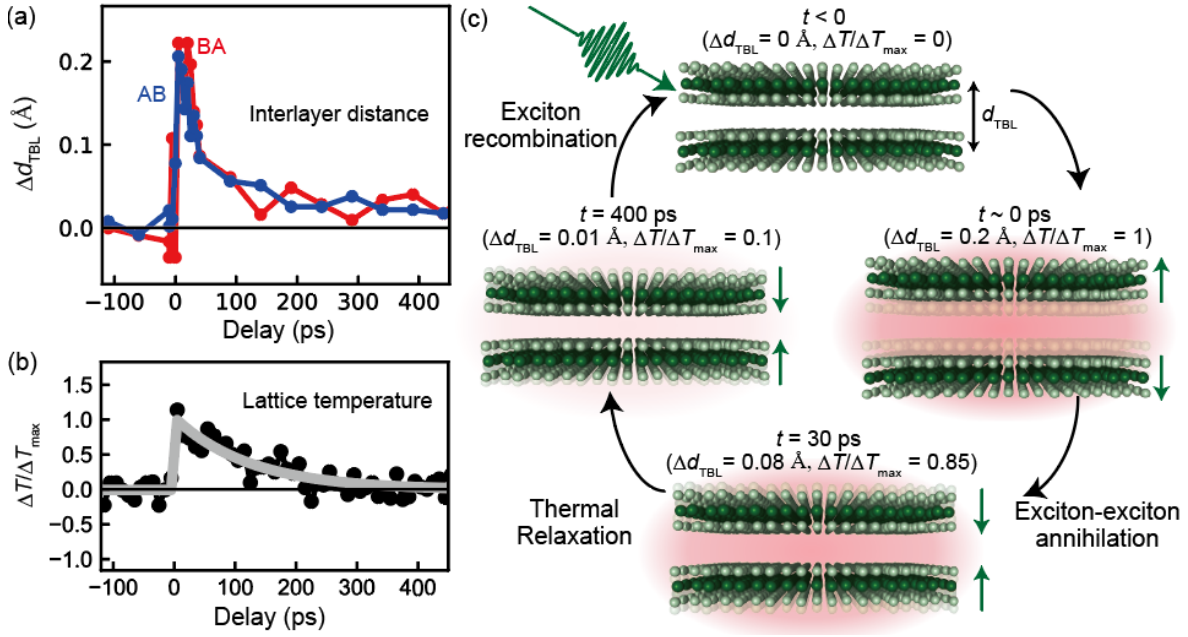
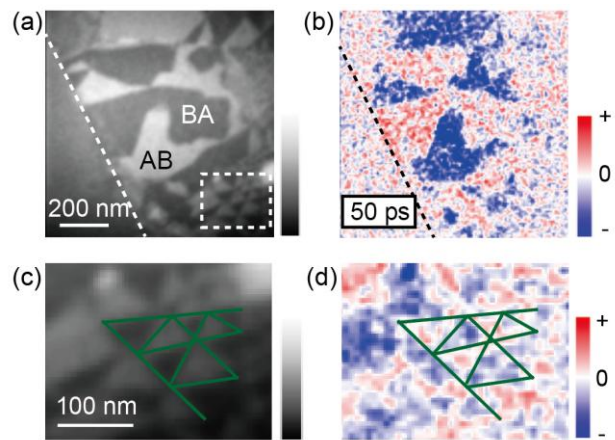


Fig. 4. (a) Time-dependence of the relative change in interlayer distance Δd_{TBL} in AB/BA stacking region estimated from the automated dark-field tomography results (see Sec. 4 in Supplemental Materials for details). (b) Time dependence of the change in lattice temperature ΔT normalized by that just after photoexcitation ΔT_{max} . The solid gray curve denotes the single exponential function with a time constant $\tau = 200$ ps [see Sec. 5 in Supplemental Materials for detail]. (c) Schematic of optically-induced interlayer decoupling in AB/BA stacking twisted-bilayer WSe₂. The interlayer distance Δd_{TBL} is changed by 0.2 Å by the photoexcitation.



Extended Data Fig. 1. (a) Dark-field image of twisted-bilayer WSe₂ before photoexcitation. The left-bottom region (below the white dashed line) is monolayer sample. (b) Relative intensity changes in the dark-field image at 50 ps after photoexcitation. (c,d) magnified view of a,b. The field of view is indicated by the white dashed rectangle in a. The green triangles are a guide for eyes.

Supplemental Materials: Layer Decoupling in Twisted Bilayer WSe₂ Uncovered by Automated Dark-Field Tomography

5 A. Nakamura^{1,2}, Y. Chiashi^{2,†}, T. Shimojima^{1,‡}, Y. Tanaka², S. Akatsuka², M. Sakano^{2,§},
 6 S. Masubuchi³, T. Machida³, K. Watanabe⁴, T. Taniguchi⁵, and K. Ishizaka^{1,2}

⁷ ¹RIKEN Center for Emergent Matter Science, Wako, Saitama 351-0198, Japan.

⁸ ²Quantum-Phase Electronics Center and Department of Applied Physics, The University of Tokyo,
⁹ Hongo, Tokyo 113-8656, Japan.

³Institute of Industrial Science, The University of Tokyo, Meguro, Tokyo 153-8505, Japan.

¹¹ Research Center for Electronic and Optical Materials, National Institute for Materials Science, 1-1
¹² Namiki, Tsukuba 305-0044, Japan

⁵Research Center for Materials Nanoarchitectonics, National Institute for Materials Science, 1-1

14 Namiki, Tsukuba 305-0044, Japan

1 **Section 1 Automated dark-field tomography and crystal structure factor
2 fitting**

3 **A. Expression of crystal structure factor S_{02}**

4 In general, crystal structure factor $S(\mathbf{q})$ is given by

5

$$S(\mathbf{q}) = \sum_i f_i(\mathbf{q}) T_i(\mathbf{q}) \exp(i\mathbf{q} \cdot \mathbf{r}_i), \quad (\text{S1})$$

6 where $\mathbf{q} = (q_x, q_y, q_z)$ is a scattering vector, $f_i(\mathbf{q})$ is atomic scattering factor, $T_i(\mathbf{q})$ is
7 Debye-Waller factor, \mathbf{r}_i is atomic position for i -th atom, and the summation takes all atoms
8 in the unit cell. For the AB stacking bilayer WSe₂, \mathbf{r}_i can be expressed as $\mathbf{r}_i = X_i \mathbf{a} + Y_i \mathbf{b} +$
9 $z_i \mathbf{e}_z$, where \mathbf{a} and \mathbf{b} are the lattice vector of twisted-bilayer WSe₂, and \mathbf{e}_z is a unit vector
10 along z axis. We define the x and z directions as the next-nearest W-W and the interlayer
11 directions, respectively [Figs. S1(a,b)]. X_i, Y_i, z_i are given in Table S1, where d_{TBL} and h_{TBL}
12 are interlayer distance and selenium height shown in Fig. S1(a). We assumed that the
13 selenium height h_{TBL} is identical for all selenium atoms, although selenium atoms inside and
14 outside of the bilayer WSe₂ are not strictly equivalent. For the BA stacking WSe₂, the sign
15 of all z_i in Table 1 should be inverted. The scattering vector \mathbf{q} for 0 2 dark-field image (\mathbf{q}_{02})
16 is given by $\mathbf{q}_{02} = (Q_1, \sqrt{3}Q_1, Q_v \tan \alpha)$, where $Q_1 = 4\pi/\sqrt{3}a$ is a length of an in-plane
17 reciprocal lattice vector, Q_v is the distance between 0 2 reciprocal lattice point and the sample
18 rotation axis [light blue arrows in Fig. S1(c,d)], and a is the lattice constant of WSe₂. When
19 the tilt rotation axis is deviated by an angle γ from the x -axis, Q_v is given as

Element	X_i	Y_i	z_i
W	0	0	d_{TBL}
W	1/3	2/3	0
Se	2/3	1/3	h_{TBL}
Se	2/3	1/3	$-h_{\text{TBL}}$
Se	1/3	2/3	$d_{\text{TBL}} + h_{\text{TBL}}$
Se	1/3	2/3	$d_{\text{TBL}} - h_{\text{TBL}}$

Table S1. \mathbf{r}_i for AB stacking WSe₂. d_{TBL} and h_{TBL} is interlayer distance and selenium height shown in Fig. S1(a)

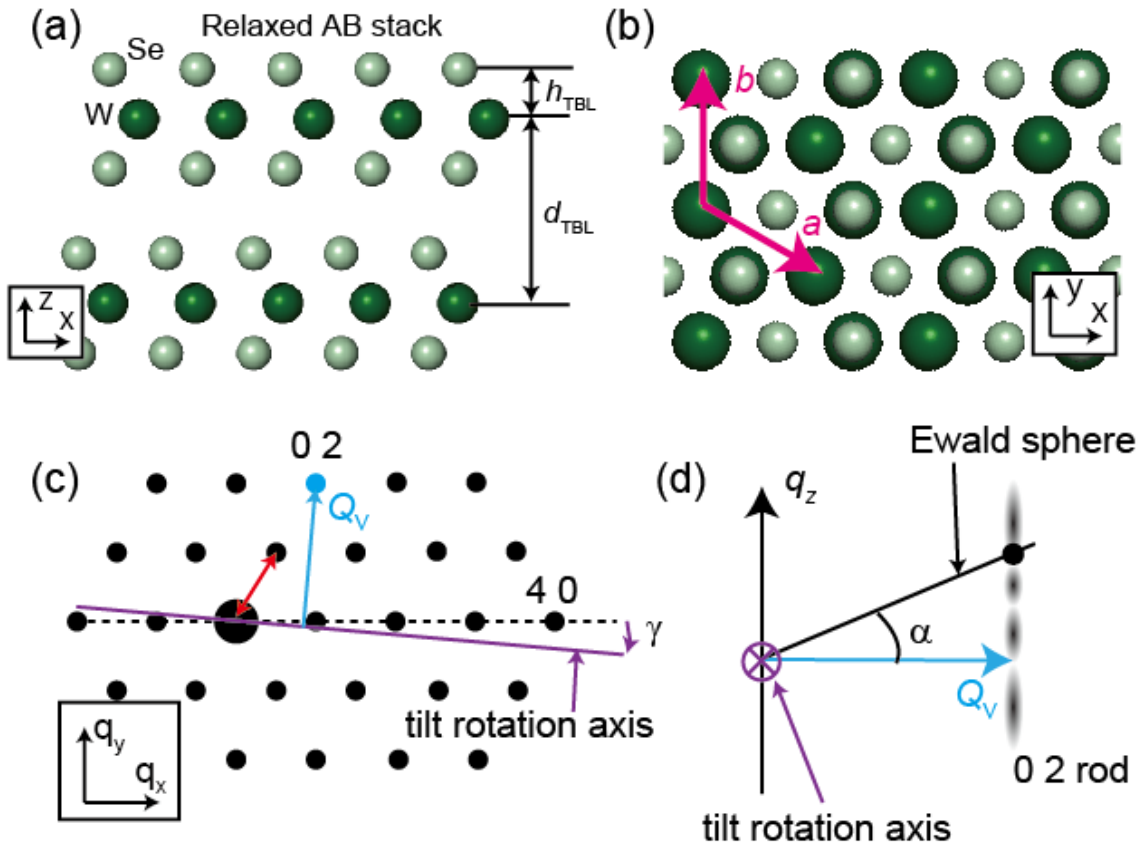


Fig. S1. (a,b) The crystal structure of the AB stacking bilayer WSe₂ and definition of x , y , and z axes. d_{TBL} and h_{TBL} are interlayer distance and selenium height. The magenta arrows in b indicate hexagonal lattice vector (\mathbf{a} and \mathbf{b}) of WSe₂, whose length $a = |\mathbf{a}| = |\mathbf{b}| = 3.32 \text{ \AA}$. (c) Schematic of reciprocal lattice points of bilayer WSe₂ in x - y plane. The sample is rotated around the purple tilt rotation axis, which is deviated from the x axis by an angle γ . (d) Schematic of 0 2 diffraction intensity profiles along the light blue line in c. The solid curve denotes Ewald sphere. \mathbf{q}_{02} is indicated by the black point.

1 $Q_1(\sqrt{3} \cos \gamma + \sin \gamma)$. γ for Sample #1 and #2 are 8.0° and 4.7° , respectively. The lattice
 2 constant $a = 3.32 \text{ \AA}$ is estimated from the electron diffraction pattern. We confirmed that the
 3 lattice constant a is not changed by temperature or photoexcitation within the present
 4 experimental error from the electron diffraction measurement. For the calculation of q_z , we
 5 approximated the Ewald sphere as a flat plane [Fig. S1(d)]. Under these assumptions, the

1 structure factor $S(\mathbf{q})$ for the 0 2 dark-field image has three free parameters: sample tilt α ,
2 interlayer distance d_{TBL} , and selenium height h_{TBL} , which we refer to as $S_{02}(\alpha, d_{\text{TBL}}, h_{\text{TBL}})$.
3 We ignored the Debye-Waller factor by setting $T_i(\mathbf{q}) = 1$, the validity of which is discussed
4 later.

5 For the equilibrium structural parameter determination by automated dark-field
6 tomography in Fig. 2, we fitted the experimental α dependence of 0 2 dark-field
7 intensity $I_{02}(\alpha)$ by $A|S_{02}(\alpha - \alpha_0, d_{\text{TBL}}, h_{\text{TBL}})|^2 + C$, where A and C are the scaling factor
8 and constant background, respectively. We added the offset of the sample tilt α_0 as a free
9 parameter because it is difficult to strictly find where $\alpha = 0$ (0 0 1 zone axes incidence of the
10 electron beam) experimentally. Both $I_{02}(\alpha)$ in AB and BA stacking regions are
11 simultaneously fitted by common $A, C, \alpha_0, d_{\text{TBL}}, h_{\text{TBL}}$. To remove the extrinsic effect of
12 fluctuating probe electron intensity, the 0 2 dark-field image intensities are normalized by
13 the intensity at the SiN region before fitting. As a result of fitting, we determined the
14 interlayer distance d_{TBL} and selenium height h_{TBL} with sub-Å (± 0.1 Å) precision, as
15 discussed in the following subsection.

16 Using the same method, we also investigated the temperature-dependent interlayer
17 distance d_{2H} for natural-bilayer 2H-WSe₂. Similarly to the AB/BA stacking of twisted
18 bilayer sample, we assumed that the selenium height h_{2H} is identical for all selenium atoms.
19 The crystal structure of 2H-WSe₂ is given in Ref. [32]. Under these assumptions, the crystal
20 structure factor S_{02}^{2H} is a function of d_{2H}, h_{2H} , and sample tilt α . We fitted the data in Fig.
21 3(b) by $A|S_{02}^{2H}(\alpha - \alpha_0, d_{2H}, h_{2H})|^2 + C$ with five free parameters $A, C, \alpha_0, d_{2H}, h_{2H}$, same as
22 the case of AB/BA stacking. The 2 0 dark-field image intensities are also normalized by the
23 intensity of the SiN region before fitting. Repeating this fitting procedure for respective
24 temperatures, we obtained temperature-dependent interlayer distance d_{2H} for the bilayer 2H-
25 WSe₂, as shown in Fig. 2.

26
27

1 **B. Error estimation and validity of approximation for Debye-Waller factor**

2 In this section, we estimate the error bar of d_{TBL} and h_{TBL} in Fig. 2(a). We consider three
 3 factors that affect the error of these parameters: Debye-Waller effect, accuracy of sample tilt
 4 offset α_0 , and uncertainty of fitting. The estimated error bar of d_{TBL} and h_{TBL} caused by the
 5 three factors are summarized in Table S2. The estimation of each value is described later in
 6 this section. Based on Table S2, we estimated the error bar of d_{TBL} and h_{TBL} in Fig. 2(a) is
 7 $\pm 0.1 \text{ \AA}$. The error of d_{TBL} (h_{TBL}) is predominantly determined by the accuracy of sample tilt
 8 (uncertainty of fitting). We found that the effect of the Debye-Waller factor is much smaller
 9 than the other two, and therefore, it is valid to approximate $T_i(\mathbf{q}) = 1$. Below we show the
 10 estimation of the error bars estimated from the three factors.

	Debye-Waller effect	Sample tilt offset	Uncertainty of fitting
Error of d_{TBL}	$< 0.01 \text{ \AA}$	0.1 \AA	0.05 \AA
Error of h_{TBL}	$< 0.01 \text{ \AA}$	0.02 \AA	0.1 \AA

Table S2. The estimated error bar of d_{TBL} and h_{TBL} caused by the three factors.

11
 12 Debye-Waller effect

13 When we consider the Debye-Waller effect, the structure factor in Eq. S1 can be
 14 expressed as

15
$$S(\mathbf{q}) = T_W(\mathbf{q}) \left[\sum_{i(W)} f_i(\mathbf{q}) \exp(i\mathbf{q} \cdot \mathbf{r}_i) + \sum_{i(\text{Se})} f_i(\mathbf{q}) \{T_{\text{Se}}(\mathbf{q})/T_W(\mathbf{q})\} \exp(i\mathbf{q} \cdot \mathbf{r}_i) \right],$$

16 where the first (second) summation takes all tungsten (selenium) atoms in the unit cell,
 17 $T_{W(\text{Se})}(\mathbf{q})$ is the Debye-Waller factor for tungsten (selenium). Therefore, the fitting result
 18 can be affected by the parameter $T_{\text{Se}}(\mathbf{q})/T_W(\mathbf{q})$. When we approximate that the thermal
 19 vibration of atoms is isotropic, $T_{\text{Se}}(\mathbf{q})/T_W(\mathbf{q})$ can be calculated from the isotropic mean
 20 square displacement $U_{\text{Se}(W)}$ as

21
$$\frac{T_{\text{Se}}(\mathbf{q})}{T_W(\mathbf{q})} = \exp \left[-\frac{|\mathbf{q}|^2 (U_{\text{Se}} - U_W)}{2} \right].$$

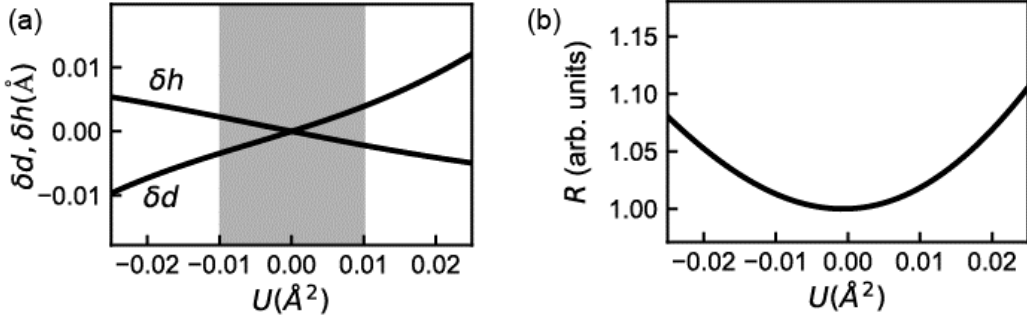


Fig. S2. (a, b) The fitting results as a function of U .

Material MX_2	T (K)	U_M (\AA^2)	U_X (\AA^2)	U (\AA^2)	Ref.
TiSe ₂	RT	0.0099	0.00718	-0.0028	[53]
MoS ₂	RT	0.00425	0.00620	0.00195	[54]
WS ₂	RT	0.00616	0.0077	0.00154	[54]
VTe ₂	RT	0.0066 ~ 0.0073	0.0079 ~ 0.0091	0.0006 ~ 0.0025	[55]
NbTe ₂	RT	0.0086 ~ 0.0091	0.0076 ~ 0.0080	-0.0015 ~ -0.0006	[56]
TaTe ₂	RT	0.0038 ~ 0.0041	0.0075 ~ 0.0106	0.0034 ~ 0.0068	[56]
WTe ₂	RT	0.0015 ~ 0.0018	0.0053 ~ 0.008	0.0035 ~ 0.0065	[57]
MoTe ₂	RT	0.0027 ~ 0.0029	0.0035 ~ 0.0006	0.0006 ~ 0.0033	[57]
TaS ₂	RT	0.0064	0.0076	0.0012	[58]
TaTe ₂	298 K	0.015 ~ 0.022	0.015 ~ 0.016	-0.007 ~ 0.0	[59]

Table S3. Atomic displacement parameters for bulk transition metal dichalcogenides. U_M and U_X are isotropic atomic displacement factor for metal and chalcogen atoms. If anisotropic atomic displacement factor U_{ij} is given in the literature, U_X and U_M are defined as one-third of the trace of the U_{ij} tensor. RT means room temperature.

1 We fitted the α dependent dark-field image intensity $I_{02}(\alpha)$ in Fig. 2(a) by changing
 2 $U \equiv U_{\text{Se}} - U_{\text{W}}$. The obtained changes in the interlayer distance $\delta d = d_{\text{TBL}}(U) - d_{\text{TBL}}(U =$
 3 0) and selenium height $\delta h = h_{\text{TBL}}(U) - h_{\text{TBL}}(U = 0)$ are shown in Fig. S2(a). In addition,
 4 we show a residual sum
 5

$$R = \sum_{i=AB,BA} \int d\alpha \left[I_{02}^i(\alpha) - \left(A |S_{02}^i(\alpha - \alpha_0, d, h)|^2 + C \right) \right]^2$$

2 as a function of U in Fig. S2(b). $I_{02}^{AB(BA)}(\alpha)$ are 0 2 dark-field image intensity $I_{02}(\alpha)$ for the
 3 AB (BA) stacking WSe₂ shown in Fig. 2(a), and $S_{02}^{AB(BA)}(\alpha, d, h)$ is the crystal structure
 4 factor for AB (BA) stacking described above. As shown in Table S3, bulk transition metal
 5 dichalcogenides typically satisfy $|U| < 0.006 \text{ \AA}^2$; therefore, U should have a similar value in
 6 twisted-bilayer WSe₂. Even if we assume $|U| < 0.01 \text{ \AA}^2$ for the twisted-bilayer WSe₂ sample,
 7 δd and δh in Fig. S2(a) are in the range of $\pm 0.01 \text{ \AA}$, which is much less than the other errors.
 8 We also note that even if we include U as a fitting parameter, $U \sim 0$ is obtained because the
 9 residual R is minimum around zero. Therefore, we conclude that the effect of the Debye-
 10 Waller factor is negligible for the present analysis. Similar crystal structure analysis in
 11 Ref. [27] also ignores the effect of the Debye-Waller factor.

13 Accuracy of sample tilt

14 Our analysis also depends on the accuracy of the tilt angle offset α_0 . We determine the
 15 upper limit of $|\alpha_0 - \alpha_0^{\text{OPT}}|$ from the experimental electron diffraction pattern, where α_0^{OPT} is
 16 optimal fitting result of α_0 . Ideally, the electron diffraction pattern should be 6-fold
 17 symmetric at $\alpha = \alpha_0^{\text{OPT}}$, where the electron beam should be strictly parallel to [001] direction.
 18 We confirmed that the electron diffraction pattern becomes asymmetric when we set $\alpha =$
 19 $\alpha_0^{\text{OPT}} \pm 0.3^\circ$. In other words, we cannot rule out the possibility that the electron beam is

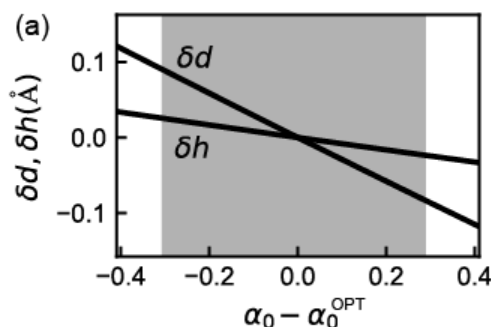


Fig. S3. Fitting results as a function of $\alpha_0 - \alpha_0^{\text{OPT}}$

1 strictly parallel to [001] direction within this range. Therefore, we estimated the upper limit
2 of $|\alpha_0 - \alpha_0^{\text{OPT}}|$ is 0.3° . Figs. S3(a,b) show the fitting results by fixing α_0 around α_0^{OPT} . The
3 other parameters, A , C , d_{TBL} , and h_{TBL} , are determined by the fitting. Both $\delta d = d_{\text{TBL}}(\alpha_0) -$
4 $d_{\text{TBL}}(\alpha_0^{\text{OPT}})$ and $\delta h = h_{\text{TBL}}(\alpha_0) - h_{\text{TBL}}(\alpha_0^{\text{OPT}})$ are changed as a function of $\alpha_0 - \alpha_0^{\text{OPT}}$.
5 Within $|\alpha_0 - \alpha_0^{\text{OPT}}| < 0.3^\circ$, δd and δh are $\pm 0.1 \text{ \AA}$ and $\pm 0.02 \text{ \AA}$, respectively, as in Fig. S3(a).

6

1 Fitting error

2 Finally, we evaluated the uncertainty of d_{TBL} and h_{TBL} practically arising when
 3 fitting the experimental data. We fixed the selenium height h_{TBL} at the values around the
 4 optimal fitting result $h_{\text{TBL}}^{\text{OPT}}$ and fitted the experimental $I_{02}(\alpha)$ in Fig. 2(a) by setting only
 5 A, C, d_{TBL} as free parameters. α_0 was fixed to the optimal value α_0^{OPT} . At $\delta h = h_{\text{TBL}} -$
 6 $h_{\text{TBL}}^{\text{OPT}} = \pm 0.1 \text{ \AA}$, the fitting result slightly deviates from the experimental value as indicated
 7 by the black arrows in Figs. S4(b,d). At $\delta h = \pm 0.2 \text{ \AA}$ [Figs. S4(a,e)], one can see the clear
 8 deviation. The $\delta d = d_{\text{TBL}}(\delta h) - d_{\text{TBL}}(\delta h = 0)$ and residual R is shown in Fig. S4(f,g).
 9 Here we determined the fitting errors by limiting the residual $R < 1.2$, as indicated by the

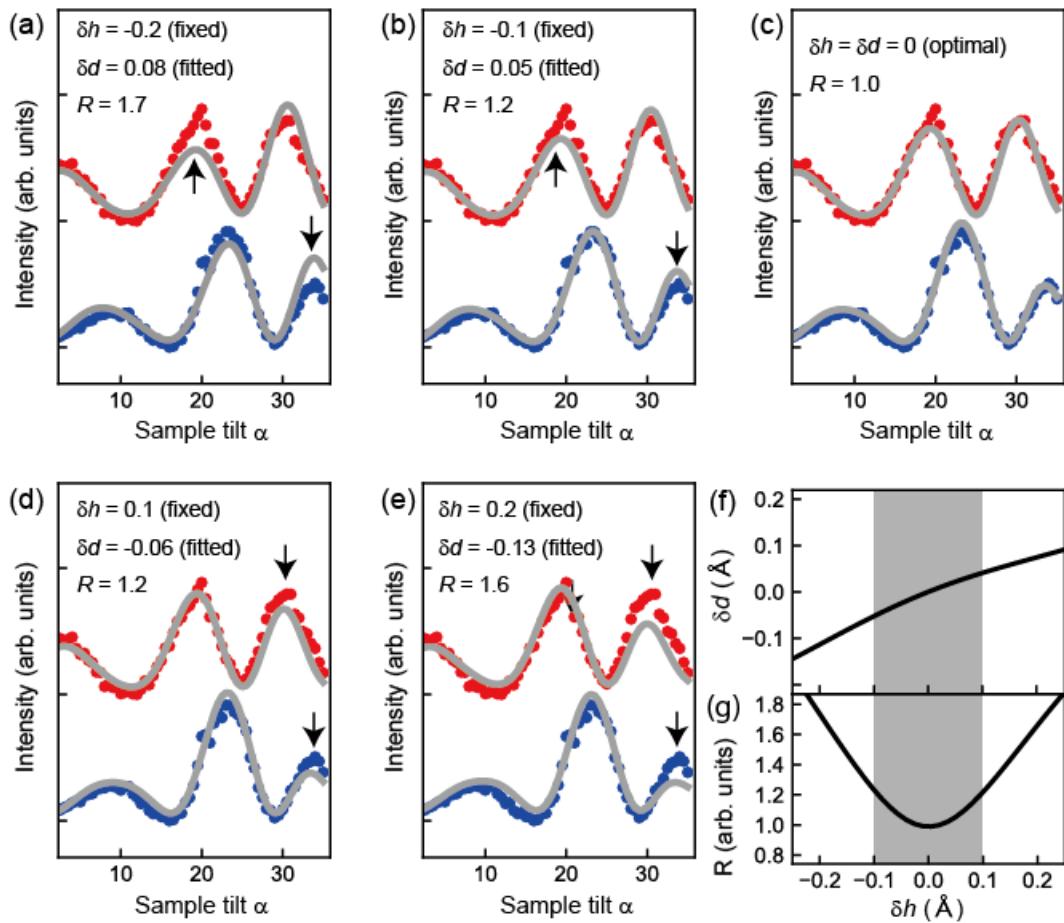


Fig. S4. (a-e) The solid curves are the fitting results for the respective h . The blue and red circles are data in Fig. 3(a). (f, g) The fitting results (d and R) as a function of h .

1 gray-shaded area. Within this consideration, the upper limit of $|\delta d|$ and $|\delta h|$ are 0.05 Å and
2 0.1 Å, respectively.

1 Section 2: Temperature-dependent automated dark-field tomography

2 This section describes the detailed temperature-dependent automated dark-field
 3 tomography measurements on twisted- and natural-bilayer WSe₂. Figs. S5(a,b) show the
 4 dark-field image intensities in the AB/BA stacking domains as a function of the sample tilt
 5 α . To obtain these data, we integrated the intensities in the blue (AB) and red (BA) rectangles
 6 in Fig. S5(c). Since it is difficult to distinguish the change between 300 K and 400 K in this

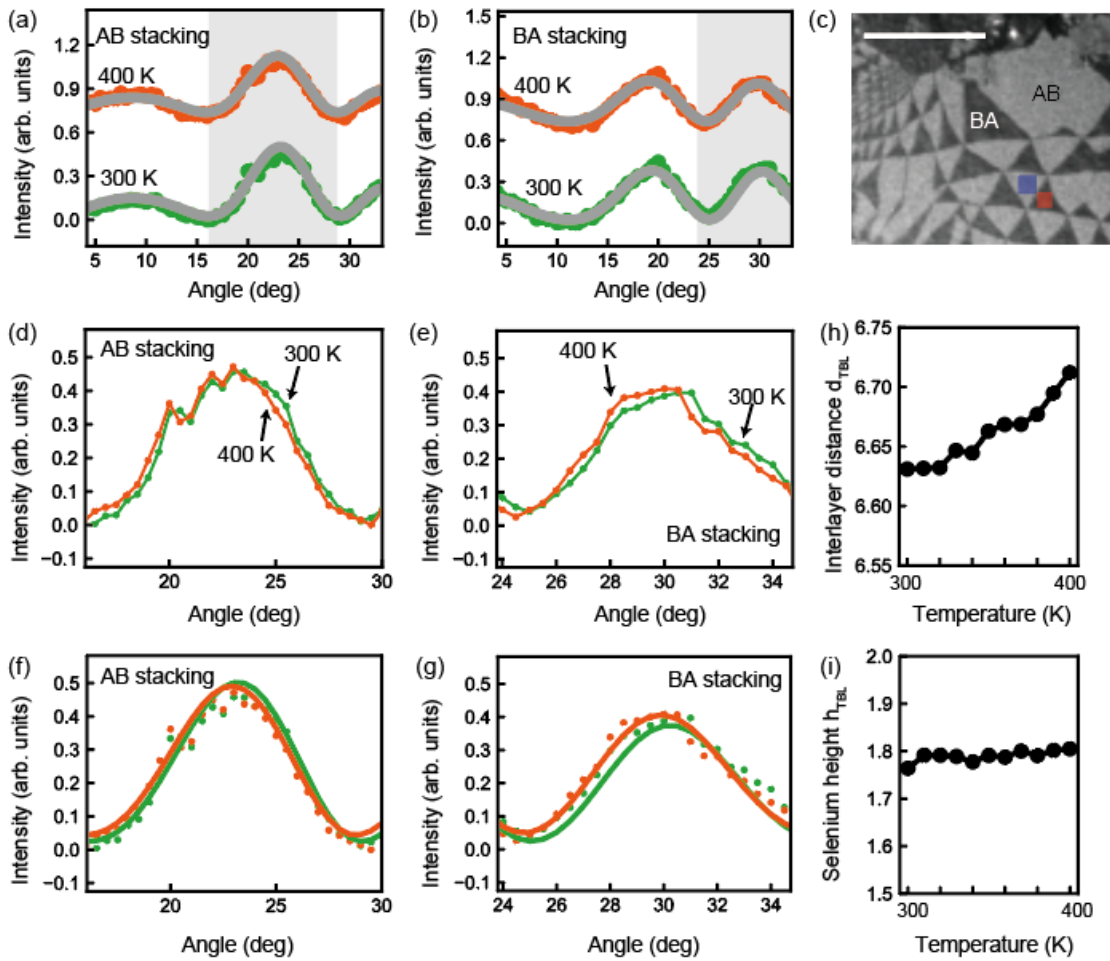


Fig. S5. (a,b) Angle-dependent 0 2 dark-field image intensities in AB and BA stacking domains at 300 and 400 K. Solid gray curves denote fitting results. (c) 0 2 dark-field image of twisted-bilayer WSe₂. (d,e) The magnified experimental data of gray-shaded regions in a, b. (f,g) The fitting results are overlaid as solid curves. (h,i) Temperature dependence of d_{TBI} and h_{TBI} .

scale, we show the magnified data in Figs. 5(d,e). In both AB and BA regions, the peak positions at around 24 and 29° are slightly shifted towards the lower angle direction at 400 K, respectively. As shown in Figs. 5(f,g), the fitting results also reflect the peak shift accordingly. As a result of the peak shift, d_{TBL} increases with heating [Fig. S5(h)], as discussed in the main text. The temperature dependence of h_{TBL} is also shown in Fig. S5(i).

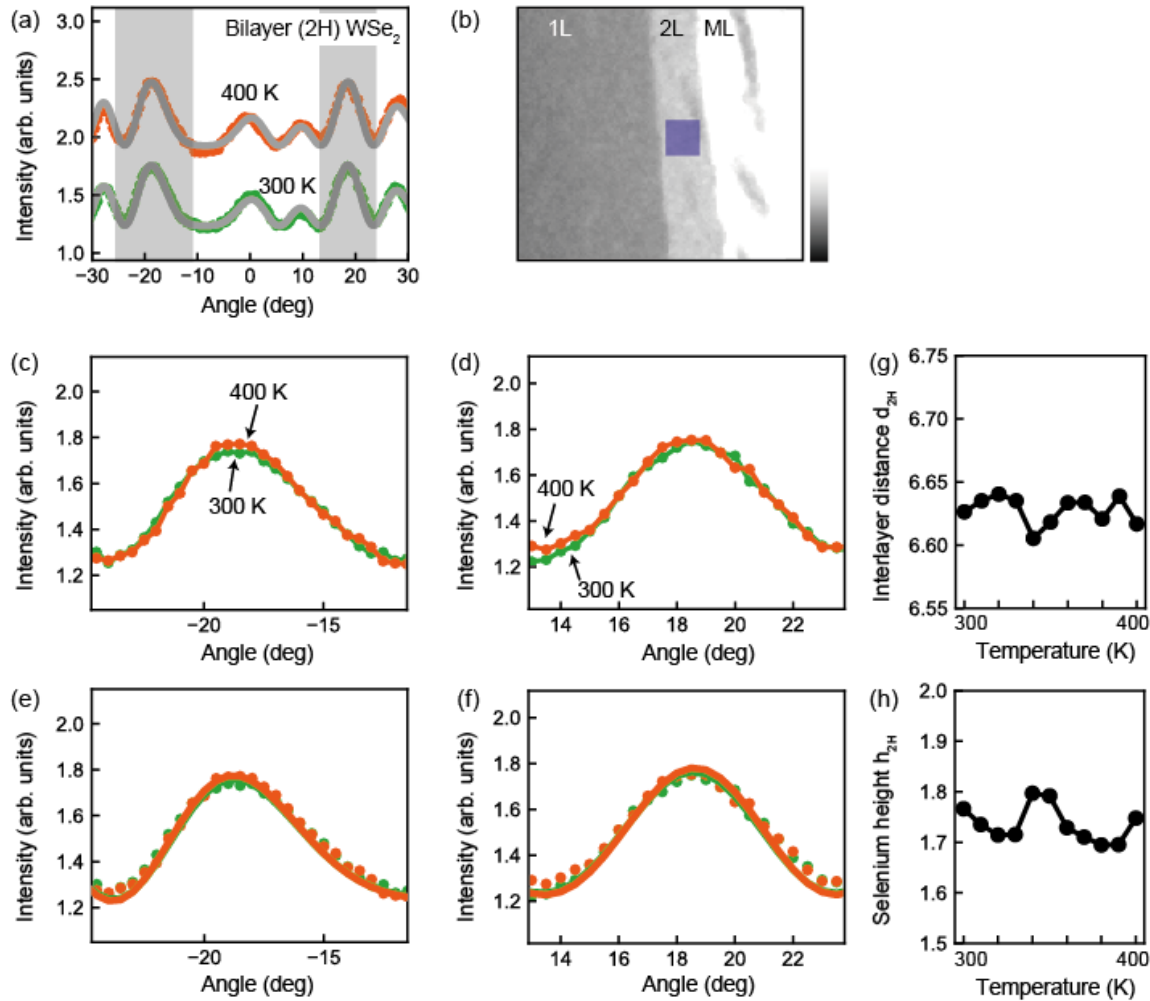


Fig. S6. (a) Angle-dependent 0 2 dark-field image intensities in natural-bilayer at 300 and 400 K. Solid gray curves denote fitting results. (b) 0 2 dark-field image of natural-bilayer WSe_2 . (c,d) Magnified experimental data of the gray-shaded regions in a. (e,f) The magnified fitting results are overlaid as solid curves. (g,i) Temperature dependence of d_{2H} and h_{2H} .

1 Fig. S6(a) shows the dark-field image intensities and fitting results for natural-bilayer
2 $2H$ -WSe₂ obtained by integrating the intensity in the blue rectangle in Fig. S6(b). We also
3 show magnified data and fitting results in Figs. S5(c-f). In contrast to the twisted-bilayer
4 WSe₂, we do not distinguish clear peak shift in natural-bilayer WSe₂. Accordingly, d_{2H} and
5 h_{2H} in Fig. S6(g,h) do not show significant temperature dependence.

1 Section 3 Characterization of Sample #2

2 We prepared Sample #2 following the procedure used for Sample #1. Figures S7(a,b)
3 show the bright- and 0 2 dark-field images of Sample #2 before photoexcitation. As described
4 in the main text, these reconstructed AB/BA stacking domains in Fig. S7(b) were stable under
5 equilibrium conditions for more than a month. However, they change abruptly and
6 irreversibly when the sample is continuously photoexcited by a sequence of 2.4 eV light
7 pulses for several days [Fig. S7(c-e)]. The AB/BA domains at the center of the image no
8 longer remain triangular after one week, and the average area of the structural domain is
9 much larger than that shown in Fig. S7(e). After one week, the structural AB/BA domain was
10 stable, and its ultrafast photoexcited dynamics could be investigated.

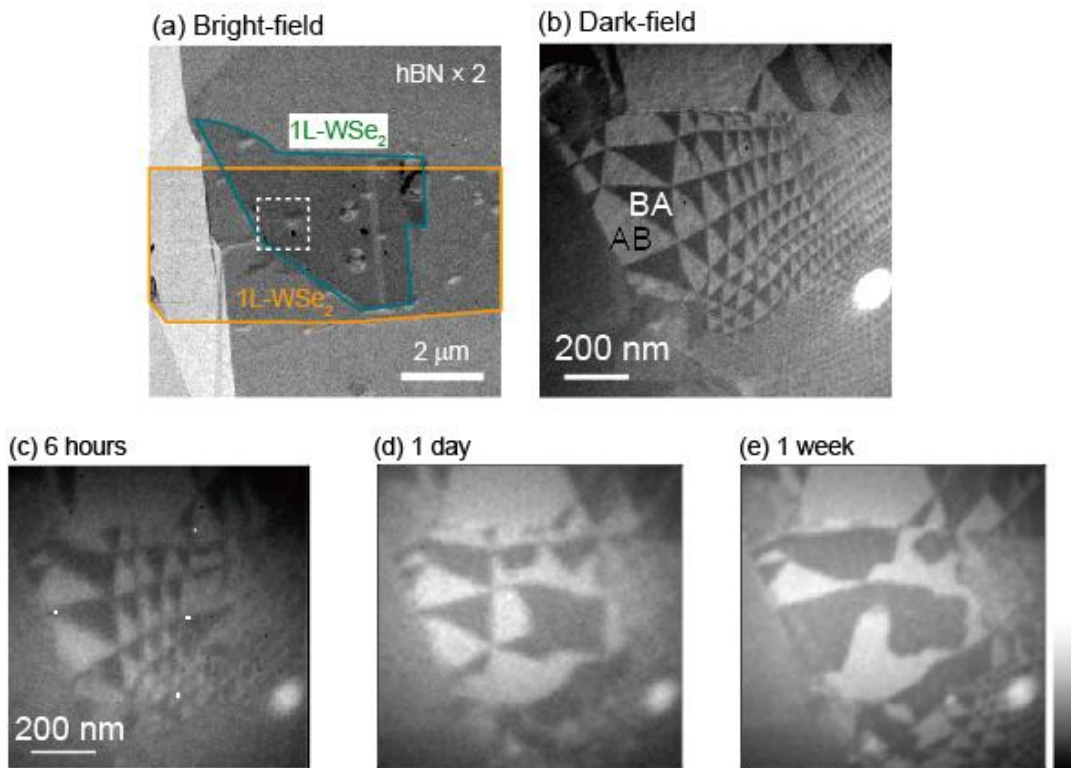


Fig. S7. (a) Bright-field image of Sample #2. (b) Dark-field image in the dashed white rectangle in a. (c-e) Gradual change in dark-field image of twisted-bilayer WSe₂ under the continuous photoexcitation by a sequence of 2.4 eV light pulses.

1 Fig. S8(a-c) shows 0 2 dark-field images of Sample #2 at several sample tilt α . The
 2 automated dark-field tomography result at AB and BA stacking in Fig. S8(d) are fitted by the
 3 structure factor following the same procedure in Sec. 1. Similarly to Sample #1, the solid
 4 curves are well-fitted to the experimental data. The obtained $d_{\text{TBL}} = 6.66 \pm 0.10 \text{ \AA}$ and
 5 $h_{\text{TBL}} = 1.64 \pm 0.10 \text{ \AA}$ are consistent with Sample #1 within the experimental error [See Fig.
 6 2(c)]. The error bars are estimated by the same procedure described in Sec. 1.

7

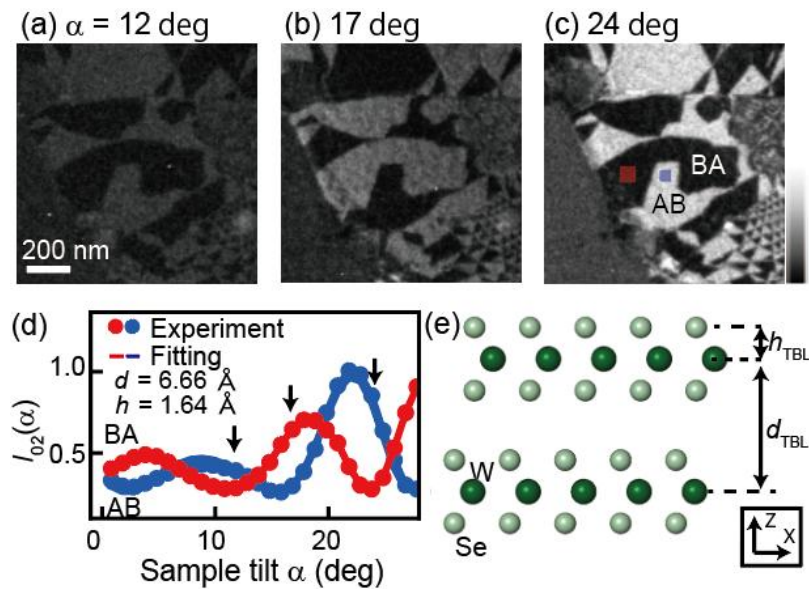


Fig. S8. (a-c) Dark-field images of twisted-bilayer WSe₂ (Sample #2) at sample tilt $\alpha = 12^\circ$, 17° , and 24° , respectively. The red and blue rectangles indicate the region where the dark-field image intensities in d is analyzed. (d) 0 2 dark-field image intensities [$I_{02}(\alpha)$] at AB and BA stacking as a function of sample tilt α . Solid curves denote fitting result. The black arrows correspond to a-c. (e) Crystal structure of AB stacking WSe₂. d_{TBL} , and h_{TBL} denote interlayer distance and selenium height from tungsten, respectively.

8

9

1 **Section 4: Evaluation of change in interlayer distance from the time-dependent data**

2 As shown in Fig. S9(a), we experimentally evaluated the 0 2 dark-field image
 3 intensity $I_{02}(t)$ for AB and BA stacking region, which we refer to as $I_{AB(BA)}(t)$ of Data 1.
 4 As discussed in Sec. 1, the intensity of the 0 2 dark-field image is approximately described
 5 by three parameters: effect of lattice temperature (Debye-Waller factor) U , interlayer distance
 6 d_{TBL} and selenium height h_{TBL} (see Sec.1 for details). Although the effect of U is limited for

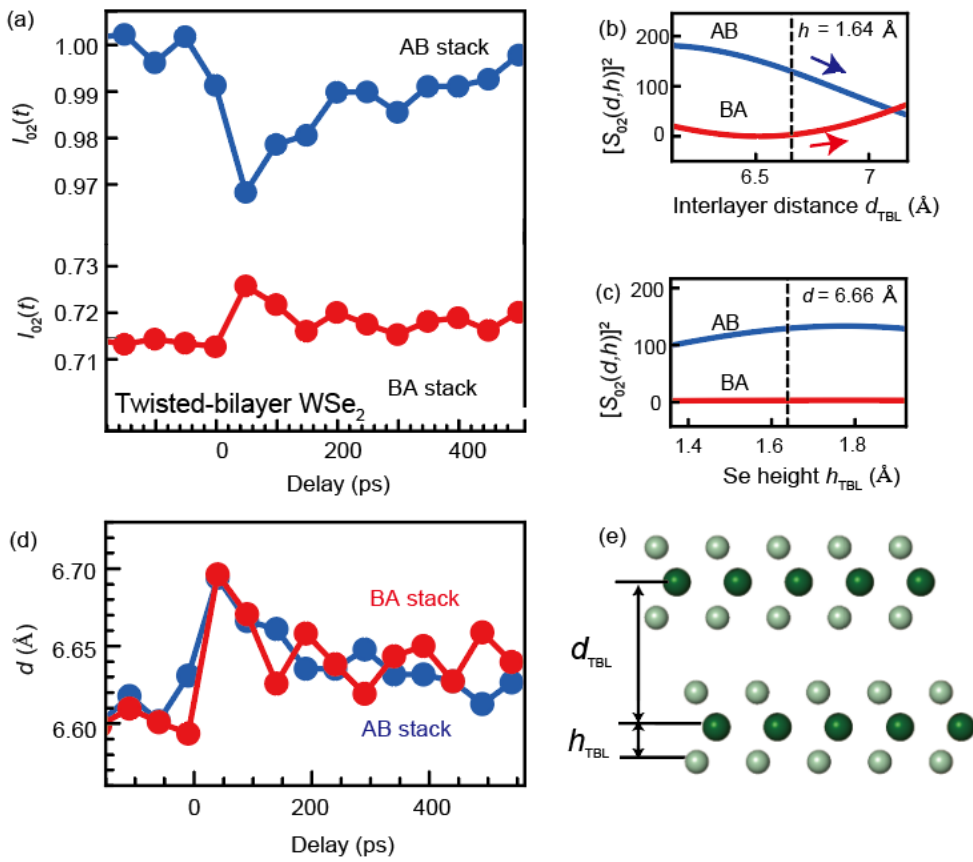


Fig. S9. (a) Time dependence of 0 2 dark-field image intensities at AB/BA stacking domains of Data 1. (b,c) Simulated dark-field-image intensity $|S(\alpha, d_{TBL}, h_{TBL})|^2$ as a function of d_{TBL} and h_{TBL} at the sample tilt $\alpha = 24.1^\circ$, respectively (See Sec. 1). The dashed lines indicate the equilibrium values determined in Sec. 3. (d) Time-dependence of the relative change in interlayer distance d_{TBL} in AB/BA stacking region estimated from the data in a. (e) Crystal structure of AB stacking WSe₂.

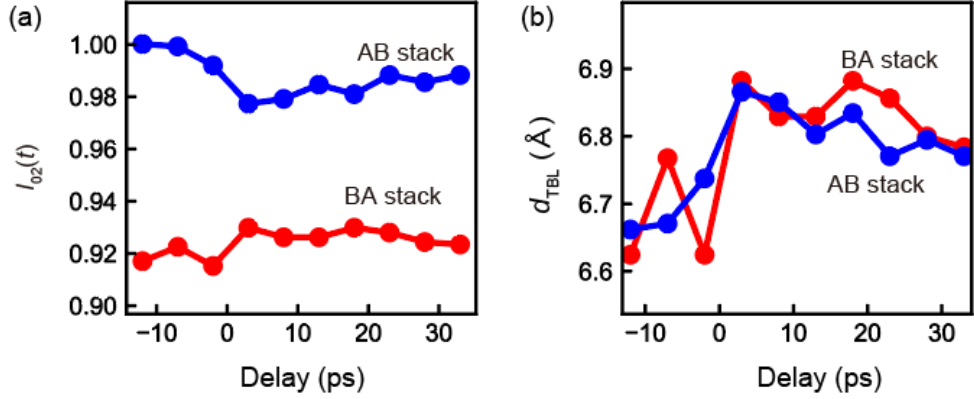


Fig. S10. (a) Time dependence of 0 2 dark-field image intensities at AB/BA stacking domains. (b) Time-dependence of the interlayer distance d_{TBL} in AB/BA stacking region estimated from the data in a.

1 the error estimation of d_{TBL} and h_{TBL} in Sec. 1, it should be considered in this section
 2 because it could affect the relative change in d_{TBL} and h_{TBL} . An increase in the dark-field
 3 image intensity at the BA stacking region cannot be described by the change in U because
 4 the Debye-Waller factor always reduces the dark-field image intensity. Therefore, the
 5 increased intensity in the 0 2 dark-field images of the BA stacking region [Fig. S9(a)] should
 6 be described by d_{TBL} and/or h_{TBL} .

7 To confirm the effect of these parameters on the 0 2 dark-field image intensity, we
 8 plotted the simulated dark-field image intensity $|S_{02}(\alpha, d_{TBL}, h_{TBL})|^2$ in Figs. S9(b,c).
 9 Although the intensity of the AB (BA) stacking decreases (increases) with the increase in the
 10 interlayer distance d_{TBL} from the equilibrium value [Fig. S9(b)], the intensity of the BA
 11 stacking is insensitive to the selenium height h_{TBL} [Fig. S9(c)]. Therefore, it can be
 12 concluded that the changes in dark-field intensity are caused by the change in the interlayer
 13 distance d_{TBL} , at least in the BA stacking region. As discussed in Sec. 1, $I_{AB(BA)}(t)$ can be
 14 approximately described by structure factor $S_{02}^{AB,BA}(\alpha, d_{TBL}, h_{TBL})$ as

$$I_{AB}(t) = A|S_{02}^{AB}[\alpha, d_{TBL}(t), h_{TBL}(t)]|^2 + C,$$

$$I_{BA}(t) = A|S_{02}^{BA}[\alpha, d_{TBL}(t), h_{TBL}(t)]|^2 + C,$$

1 where A and C are the scaling factor and constant background intensity. The sample tilt $\alpha =$
 2 24.1° is fixed during the time-dependent measurements. Using these relations, we can
 3 determine A and C from $I_{AB}(t < 0)$, $I_{BA}(t < 0)$, $d(t < 0) = 6.66 \text{ \AA}$ and $h(t < 0) = 1.64 \text{ \AA}$
 4 in Sec. 3. After determining A and C , we can determine time dependence of d_{TBL} at $t > 0$ by
 5 compare Fig. S9(a) with Figs. S9(b) under the assumption that $h_{\text{TBL}}(t)$ is constant in AB
 6 stacking domain. It is noted that we do not impose any assumption on $h_{\text{TBL}}(t)$ in BA stacking
 7 domain because $I_{BA}(t)$ is insensitive to $h_{\text{TBL}}(t)$ as described above. In both AB and BA
 8 regions, the estimated interlayer distance d_{TBL} is increased by about 0.1 \AA . The time
 9 dependence of d_{TBL} in the AB and BA regions is consistent, suggesting that the change in
 10 intensity in AB stacking is also primarily dominated by d_{TBL} , supporting the assumption.
 11 The similarity between AB and BA stacking is expected because the crystal structures of AB
 12 and BA stacking are identical. Thus, the photoexcited processes in these two regions may not
 13 be very different.

14 Similarly to Fig. S9, we performed the same analysis on the 0 2 dark-field image
 15 intensity in Fig. S10(a) (Data 2) and obtained the time dependence of d_{TBL} as shown in Fig.
 16 S10(b). In Data 2, we use a $40 \mu\text{m}$ objective aperture larger than that of Data 1 ($20 \mu\text{m}$). As
 17 a result, the background intensity (Intensity at $t < 0$ in BA stacking region, 0.92) is
 18 significantly increased as compared to Data 1 (0.713). Therefore, it is impossible to compare
 19 these results directly. To remove the contribution from the background and compare the
 20 results, we use normalized dark-field image intensity

$$21 \quad \bar{I}_{02}^i(t) = \frac{I_{02}^i(t) - I_{02}^{BA}(t < 0)}{I_{02}^{AB}(t < 0) - I_{02}^{BA}(t < 0)},$$

22 where $i = AB, BA$. This normalized intensity satisfies $\bar{I}_{02}^{AB}(t < 0) = 1$ and $\bar{I}_{02}^{BA}(t < 0) = 0$,
 23 as confirmed in Fig. 3(g). Both $\bar{I}_{02}^i(t)$ and estimated $d_{\text{TBL}}(t)$ from Data 1 and 2 are smoothly
 24 connected, as seen in Fig. 3(g). It is also noted that the $d_{\text{TBL}}(t)$ in AB and BA stacking is
 25 almost consistent within the experimental error, which again supports the assumption that
 26 $h_{\text{TBL}}(t)$ is constant in AB stacking domain.

27

Section 5 Estimation of transient lattice temperature

We estimated the transient lattice temperature of the twisted-bilayer WSe₂ (Sample #2) from ultrafast diffraction measurements. Figure S11(a) shows the diffraction pattern of the tilted ($\alpha = 24.1^\circ$) twisted-bilayer WSe₂, where we observe six-fold Bragg peaks that originate from the twisted-bilayer WSe₂ and several bright Bragg peaks that arise from hBN. We set the field of view to be much larger ($\sim 5 \mu\text{m}$) than the AB/BA stacking domain size ($\sim 100 \text{ nm}$), and thus both AB/BA stacking domain is almost equivalently averaged. When the sample was photoexcited, the intensity of most Bragg peaks decreased [Fig. S11(b)]. Such a decrease in the Bragg peak intensity implies the increased lattice temperature because the Debye-Waller factor always reduces the Bragg peak intensity. In particular, 4 0 diffraction is located near the rotation axis of the sample [horizontal red dashed line in Fig. S11(a)], and

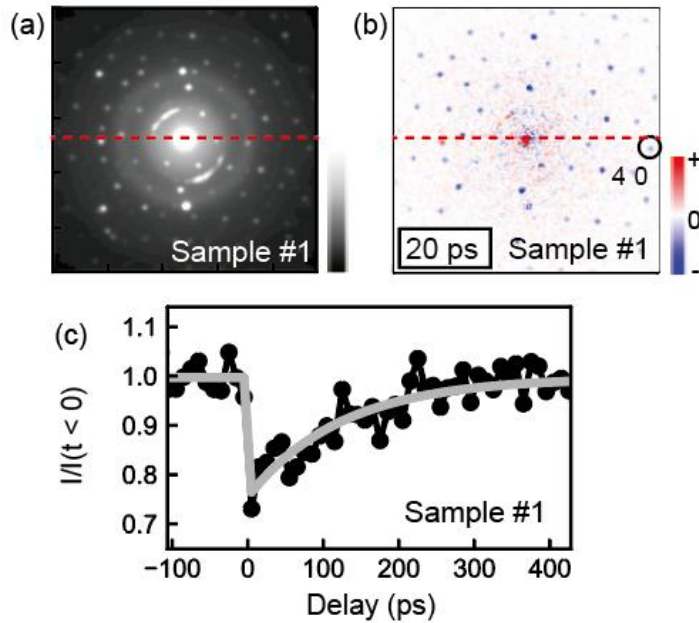


Fig. S11. (a) Diffraction pattern of twisted-bilayer WSe₂ before photoexcitation. The red dashed line is the axis of rotation for sample tilt α . Several bright Bragg diffraction spots, such as indicated by red arrow, originating from hBN are observed in addition to the hexagonal pattern from WSe₂. (b) Relative intensity changes at 20 ps after photoexcitation. (c) Time dependence of 4 0 diffraction intensity. All figures are identical with Extended Data Fig. 3.

1 therefore, the z component of the scattering vector (q_z) should be almost zero [see Sec. 1].
 2 Under such a condition, the intensity of 4 0 Bragg diffraction is not affected by structural
 3 changes because the free parameters of the WSe₂ crystal, d_{TBL} , and h_{TBL} , move atoms along
 4 the z direction (note that the crystal structure factor $S(\mathbf{q})$ in Eq. S1 does not depend on d_{TBL}
 5 and h_{TBL} when $q_z = 0$). We confirmed that the relative 4 0 diffraction intensity

$$6 \quad \Delta I_{40} = \frac{|S_{40}^{AB}(d_{\text{TBL}} + \Delta d_{\text{TBL}})|^2 + |S_{40}^{BA}(d_{\text{TBL}} + \Delta d_{\text{TBL}})|^2}{|S_{40}^{AB}(d_{\text{TBL}})|^2 + |S_{40}^{BA}(d_{\text{TBL}})|^2}$$

7 (we omitted α and h_{TBL} for clarity) is 0.987 when $\Delta d_{\text{TBL}} = 0.2$ Å, $d_{\text{TBL}} = 6.66$ Å, $h_{\text{TBL}} =$
 8 1.64 Å, and $\alpha = 24.1^\circ$. Therefore, change in the interlayer distance does not significantly
 9 affect the 4 0 diffraction intensity. In Fig. S11(c), the time-dependence of the 4 0 Bragg
 10 intensity decreases by $\simeq 25\%$ at 5 ps after photoexcitation and then relaxes to an equilibrium,
 11 which should be interpreted as an increase in transient lattice temperature. We fitted the curve
 12 in Fig. S11 by a single exponential function $\exp(-t/\tau)$. The fitting result (solid gray curve)
 13 well reproduces the experimental result with a time constant of 200 ps, which is different
 14 from the fast (50 ps) component of time-dependent interlayer distance in Fig. 4(a). As the
 15 Debye-Waller factor $T_i = \exp(-|\mathbf{q}|^2 U_i)$ is approximately proportional to the transient
 16 lattice temperature $T (\propto U_i)$ within $U_i < 0.01$ (see Sec. 1), we assume the change in 4 0
 17 diffraction intensity is proportional to the change in lattice temperature ΔT . Under this
 18 assumption, we translated $\Delta I(t)/I(t < 0)$ to $\Delta T/\Delta T_{\text{max}}$ in Fig. 4(b) as $\Delta T(t) = \Delta I(t)/$
 19 $I(t < 0)$ and $\Delta T_{\text{max}} = \max \Delta T(t)$. It is noted that we used the fitting results instead of
 20 experimentally obtained $\Delta I(t)/I(t < 0)$. Although we cannot eliminate the effect of the
 21 thermal expansion in the slow component, the fast component cannot be described by the
 22 transient lattice temperature at least.

23